CHAPTER NINE

Some Theoretical and Numerical Approaches to the Optics of Fractal Smoke

VADIM A. MARKEL

Department of Electrical Engineering, Washington University, St. Louis, MO 63130

VLADIMIR M. SHALAEV

Department of Physics, New Mexico State University, Las Cruces, NM 88003

THOMAS F. GEORGE

University of Wisconsin-Stevens Point, Stevens Point, WI 54481

9.1. INTRODUCTION

Investigation of the optical properties of carbonaceous smoke produced by incomplete combustion of different types of fuels or wild fires has practical importance for many application areas, such as climate research and remote sensing of fires, to name just a few. Very active and vigorous research into the optical properties of smoke has been conducted over the past 30 years. Many of the experimental and theoretical questions are now resolved. The geometrical structure and chemical composition of soot aggregates has been studied in detail (see Chapter 10), and many analytical and numerical methods for calculating the optical characteristics and for obtaining physical properties of smoke from optical measurements have been developed. However, there are several factors that preclude this topic from being closed.

Most of the quantitatively accurate results in the visible and near-infrared (IR) spectral regions appeared only recently, as increasingly powerful computers became available. However, when the wavelength is further increased, the electromagnetic (EM) interaction of small carbon nanospheres that comprise soot particles becomes stronger and more important, and so becomes important the geometrical structure of soot. This importance was demonstrated by Bruce et al. [1] who measured optica

Optics of Nanostructured Materials, Edited by Vadim A. Markel and Thomas F. George
ISBN 0-471-34968-2

characteristics of diesel soot from the visible to the centimeter wavelength range. Unfortunately, most analytical and numerical methods become less effective, or even not applicable, when the interaction of primary nanospheres becomes strong. This fact is, of course, evident for perturbative methods that treat such interaction as a perturbation. But this is also true for nonperturbative numerical methods based on the multipole expansion of fields scattered by each nanosphere and satisfying boundary conditions at each surface of discontinuity. Generally, such approaches lead to an infinite system of linear equations with respect to the unknown expansion coefficients, which has to be truncated. After the truncation, its dimensionality is $\sim N(L+1)^2$, where N is the number of monomers in a soot cluster and L is the maximum order of the spherical harmonics involved in the expansion. As will be illustrated below, the value of L required for satisfactory convergence of the method grows with the wavelength, and eventually makes obtaining a numerical solution not feasible. In this chapter, we will discuss a nonperturbative method based on the geometrical renormalization of clusters. This method allows one to stay within the dipole approximation ($L = 0$) and, therefore, lacks the numerical complexity of the full multipole expansion.

Another reason why research into the optics of carbonaceous soot is far from being completed is the complexity of the object. Indeed, most of the results obtained in the literature assume the simplest geometrical structure and composition of soot clusters. In practice, soot is much more complicated, both geometrically and chemically. In the atmosphere, soot can interact and form agglomerates with moisture and other chemical elements, which can lead to restructuring and a significant change in optical properties. Chapter 10 is largely devoted to this circle of problems, as well as to experimental and theoretical aspects of studying the soot structure variability and its implications for optical properties.

In this chapter, we focus on analytical and numerical approaches to calculating optical properties of fractal smoke with a simple fractal structure and optical constants that are assumed to be known. Thus, we will consider a purely EM problem, leaving a lot of complexity that is characteristic to the physical properties of soot out of our discussion. However, two introductory sections give a brief review of the geometrical properties and optical constants of fractal soot, since they are used in numerical examples throughout the chapter. In Sections 9.5 and 9.6 we will consider two topics that are, in a sense, nontraditional: fluctuations of light intensity scattered by random smoke aggregates and the absorption of light by the smoke clusters placed inside water microdroplets, both in the first Born approximation.

9.2. GEOMETRICAL PROPERTIES

It has been long recognized that smoke usually consists of agglomerates of hundreds or thousand of small, nearly spherical particles (monomers) with typical radii varying from 10 to 50 nm, depending on the origin of the smoke [1–6]. The distribution of monomer sizes for a specific type of smoke is, however, significantly more narrow,

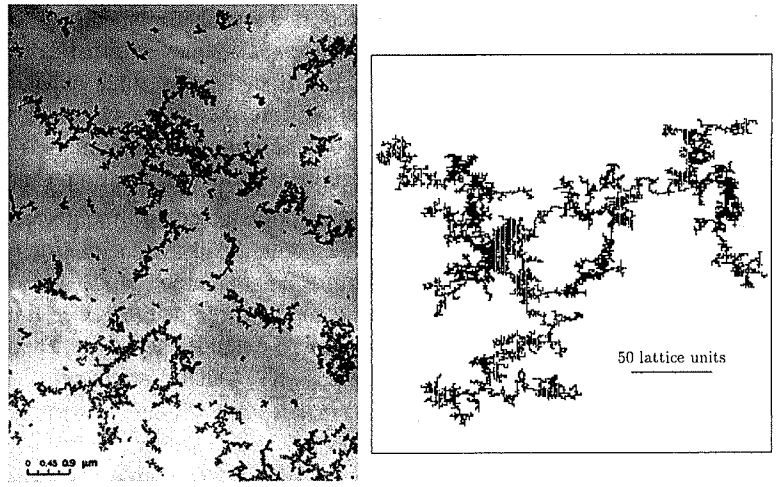

(a) (b)

Figure 9.1. Experimental (a) (Courtesy of E. F. Mikhailov, S. S. Vlasenko, and A. A. Kiselev) and computer-generated (b) smoke clusters.

and it is customary to assume that the diameters of the spherical monomers are the same. A sample micrograph of several smoke agglomerates is shown in Fig. 9.1(a). The reader will recognize that smoke clusters have fractal geometry. This fact was verified experimentally by digitization of electron micrograph images similar to the one shown in Fig. 9.1(a) [3,5,7–9] and by scattering experiments [7,8,10,11]. The value of fractal dimension D was shown to be close to 1.8.

The geometrical structure of smoke aggregates is most often simulated using the cluster–cluster aggregation model introduced by Meakin [12] and Jullien et al. [13]. In this model, monomers are sparsely and randomly distributed in space at the initial moment of time and, then, allowed to move via Brownian trajectories, sticking on contact. The subclusters formed in this process continue to move, colliding and sticking with other subclusters and isolated monomers, until large agglomerates are formed. A sample computer-generated cluster–cluster aggregate is shown in Fig. 9.1(b). The Meakin model accurately describes the statistical properties of soot because it captures the most important features of the real aggregation process: subclusters of various sizes and individual particles move in space simultaneously and independently, there is no fixed center of aggregation, and the dependence of mobility of individual subclusters on their mass can be easily taken into account in simulations.

Although the visual resemblance of the experimental and computer-generated samples in Fig. 9.1 is more or less apparent, a comparison is complicated due to the random nature of the smoke agglomerates. Therefore, it is essential to study the statistical characteristics of the clusters. One of the most important of such characteristics, from the point of view of optical properties, is the pair density–density

correlation function $p(r)$, which can be defined as the probability density to find a pair of distinct monomers separated by the distance r. The Fourier transform (FT) of $p(r)$ gives the optical structure factor [14]. For fractals, this function obeys the power-law dependence on r in the so-called intermediate asymptote region $l \ll r \ll R_g$, where l is the distance between two neighboring monomers (referred to as the "lattice unit" below), and R_g is the cluster radius of gyration, defined as $R_g = \sqrt{\langle(\mathbf{r}_i - \mathbf{R}_{cm})^2\rangle}$, with $\mathbf{r}_i$ and $\mathbf{R}_{cm}$ being the radius vectors of the ith monomer in a cluster and of the cluster's center of mass. In fact, the above inequalities do not need to be especially strong (usually, the factor of 2 is sufficient), and since most of the physically important integrals involving $p(r)$ converge at the lower limit, the region of applicability of the scaling formula can be extended to $r = 0$. Then, for a monodisperse ensemble of random soot clusters, $p(r)$ can be written in the most general form as

$$p(r) = \frac{ar^{D-1}}{Nl^D} f\left[\frac{r}{R_g(N)}\right] \qquad \int_0^\infty p(r)dr = 1 \tag{9.1}$$

where N is the number of monomers in a cluster, a is a numerical constant of the order of unity, D is the fractal dimension, and $f(x)$ is the cutoff function, such that $f(0) = 1$, $|df(0)/dx| < \infty$. The two-point correlation function found numerically in [15] is shown in Fig. 9.2(a).

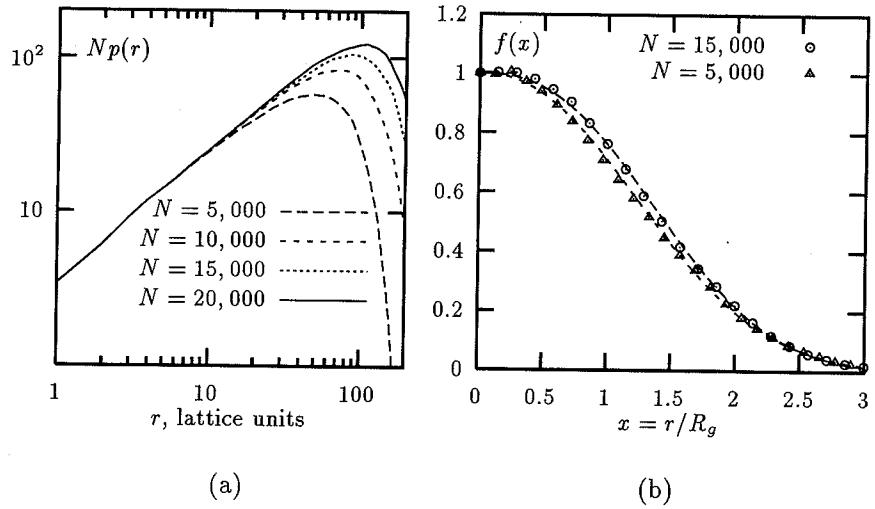

Figure 9.2. Two-point correlation functions $p(r)$ for cluster–cluster aggregates with different numbers of particles N (a) and the corresponding cutoff function $f(x)$ (b). In (b), dashed lines correspond to the generalized exponential cutoff of the form $f(x) = \exp(-\alpha x^\beta)$, and the centered symbols (circles and triangles) correspond to the numerical calculations. The values of the constants are $\alpha = 0.344$; $\beta = 2.238$ for $N = 5000$; and $\alpha = 0.273$, $\beta = 2.489$ for $N = 15{,}000$.

The dependence of the gyration radius on N is also governed by the fractal dimension,

$$R_g(N) = blN^{1/D} \tag{9.2}$$

where b is another dimensionless constant.

In a recent numerical study [15], we found that the constants D determined from Eqs. (9.1) and (9.2) can be slightly different.[1] We have also evaluated the constants a and b numerically for computer-generated cluster–cluster aggregates and found that $a \approx 4$ and $b \approx 0.6$, which is in qualitative agreement with other studies. We estimate from the data of Mountain and Mulholland [17], Cai et al. [8,11], and Oh and Sorensen [18], that $b \approx 0.4$. The values of a constant related to b (and of the fractal dimension) obtained from numerical simulations by different authors were reviewed by Wu and Friedlander [19], with b varying in the range from 0.25 to 0.5. It should be noted that while the formulas (9.1) and (9.2) are quite universal, the specific values of a and b can vary depending on the regime of aggregation. They are also sensitive to the number of primary particles employed in numerical calculations. In our calculations, the maximum value of N employed for the numerical fitting of (9.2) was 20,000, which is significantly larger than the maximum N in the set of data presented by Wu and Friedlander [19] ($N_{max} = 500$). The dependence on N can be explained by the phenomenon of multiscaling, when the characteristic constants can slowly depend on N.

Significantly less information can be found on the constant a. However, when the form of the cutoff function $f(x)$ is specified, a is not an independent constant because of the normalization condition. The combination ab^D is fixed and can be calculated from the form of the cutoff function. We have estimated that $ab^D \approx 1.6$ [15].

When the physically important integrals involving $p(r)$ converge at the upper limit while r is still smaller than R_g, and the value of the cutoff function in (9.1) does not deviate significantly from unity, the knowledge of the exact form of the cutoff function $f(x)$ is not necessary. This was illustrated by Berry and Percival [20] in the frame of the mean-field approximation, and we will see such examples below. But in general, the form of $f(x)$ influences the optical properties. The well-known example is the first Born approximation for the differential scattering cross-section for the "intermediate" values of the transmitted wavevector $q = |\mathbf{k} - \mathbf{k}'| \sim 1/R_g$ [14]. The most frequently discussed forms of $f(x)$ are the generalized exponential $f(x) = \exp(-\alpha x^\beta)$ (the Gaussian cutoff is the particular case $\beta = 2$) and the so-called overlapping spheres cutoff $f(x) = (x - x_0)^2(x + 2x_0)/2x_0^3$ if $x < x_0$, which is the exact analytic cutoff for a random nonfractal gas of particles enclosed in a spherical volume.

Mountain and Mulholland found numerically that $f(x)$ is of a generalized exponential form with $\alpha = 0.2$ and $\beta = 2.5$ [17]. Sorensen and co-workers studied the cutoff functions by analyzing electron micrographs of soot clusters [11] and also indirectly by analyzing light scattering data [21,22] (with the interpretation of the

[1] This phenomenon is related to multiscaling [16].

scattering data based on the first Born approximation) and found that $f(x)$ is decaying with x much faster than exponentially, with the Gaussian cutoff being a fairly good approximation. Our numerical results, which are in qualitative agreement with the above references, also confirm the generalized exponential form of $f(x)$ with coefficients α and β exhibiting a slow systematic dependence on the number of monomers N. An example of generalized exponential fit to the numerically calculated $f(x)$ is shown in Fig. 9.2(b) (see the figure caption for details).

To conclude this section, we briefly discuss higher order correlation functions. They naturally appear in higher orders of the perturbation theory, or when fluctuations of the optical characteristics (rather than the ensemble-average quantities) are considered [15,23]. In a Gaussian medium, all higher order correlation functions can be expressed analytically through the second-order correlators [24]. This fact significantly simplifies the diagrammatic technique in the perturbation expansion of the mean field for wave propagation in a random Gaussian medium [25]. However, as we have verified numerically, fractal cluster–cluster aggregates are not Gaussian [15]. Because of the many similarities between the computer-generated cluster–cluster aggregates and real smoke clusters, it is reasonable to believe that this conclusion is also true for real smoke. As an example, we have studied in detail the reduced four-point correlation function $p_4(r)$, which is important for describing the deviations of scattered intensity from the average due to the random nature of clusters (see Section 9.5). The correlator $p_4(r)$ is defined as the probability density to find the distance $|\mathbf{r}_i - \mathbf{r}_j + \mathbf{r}_k - \mathbf{r}_l|$ [$i \neq j$, $k \neq l$, and any of the pair of indexes (i, j) can coincide with any of the pair (k, l)]. It was found that $p_4(r)$ is not described by a scaling formula with a cutoff similar to (9.1), but is given by a

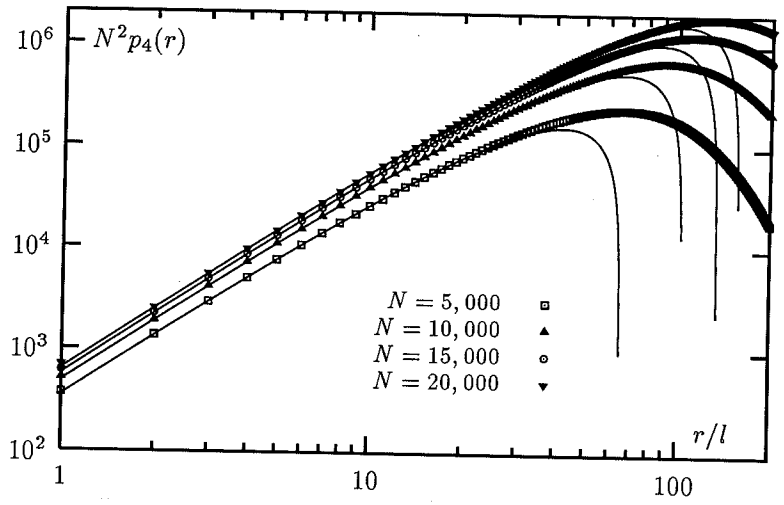

Figure 9.3. Four-point correlation function $p_4(r)$ calculated numerically (centered symbols) and from the analytic expression (1.3) with $n = 2$, $c_0 \approx c_1 \approx 23$ (solid line) for different N. The gyration radius R_g changes from $\approx 50l$ for $N = 5000$ to $\approx 100l$ for $N = 20{,}000$.

series of the form

$$p_4(r) = \frac{r^2}{N^{3/D}l^3} \sum_{k=0}^{n} (-1)^k c_k \left(\frac{r}{R_g}\right)^{k(2D-3)} \tag{9.3}$$

where c_k are dimensionless positive coefficients that have to be determined numerically. Approximation of $p_4(r)$ by the expression (9.3) is illustrated in Fig. 9.3. By increasing the number of terms n in (9.3), it is possible to fit $p_4(r)$ for increasingly higher values of r. The important feature of (9.3) is that the coefficients c_k do not depend on N (apart from a very weak multiscaling dependence) and are in that sense universal, which distinguishes (9.3) from an arbitrary power expansion. Another important feature of Eq. (9.3) is that $p_4(r)$ cannot be described by a universal scaling behavior with a cutoff function of the type $p_4(r) = r^2 f(r/R_g)/N^{3/D}l^3$. Although a function $f(x)$ can be found from (9.3), its first derivative diverges at $x = 0$ for $D < 2$ (one of the requirements for the cutoff function is a finite derivative at $x = 0$).

9.3. OPTICAL CONSTANTS OF CARBON SMOKE

Dalzell and Sarofim [26] studied the optical constants of several soots using reflectance measurements. They suggested a dispersion formula that describes experimental measurements quite accurately and is based on the well-known quantum expression for the complex dielectric function

$$\varepsilon(\omega) = 1 - \sum_n \frac{f_n^2}{\omega^2 - \omega_n^2 + i\gamma_n\omega} \tag{9.4}$$

Earlier, Taft and Philipp [27] identified experimentally three optical resonances in graphite, two of which correspond to bound electrons and one to a conduction electron. The resonance frequencies are $\omega_c = 0$ (conduction electron), $\omega_1 = 1.25 \times 10^{15}\ \mathrm{s}^{-1}$ and $\omega_2 = 7.25 \times 10^{15}\ \mathrm{s}^{-1}$ (or corresponding wavelengths: $\lambda_c = \infty$, $\lambda_1 = 1.51\ \mu\mathrm{m}$, $\lambda_2 = 0.26\ \mu\mathrm{m}$). The values of the relaxation constants were found to be $\gamma_c = \gamma_1 = 6.00 \times 10^{15}\ \mathrm{s}^{-1}$, $\gamma_2 = 7.25 \times 10^{15}\ \mathrm{s}^{-1}$. Dalzell and Sarofim [26] assumed that the same electronic transitions contribute to the dielectric constant of carbon soot and used the above values of ω_n, γ_n to fit the formula (9.4) to their experimental data treating f_n, which depend on the concentration of optically active electrons, as free parameters. A very accurate fit to the experimental data for propane soot was achieved for the following values of f_n: $f_c = 4.04 \times 10^{15}\ \mathrm{s}^{-1}$, $f_1 = 2.93 \times 10^{15}\ \mathrm{s}^{-1}$, $f_2 = 9.54 \times 10^{15}\ \mathrm{s}^{-1}$ in the spectral range $0.4\ \mu\mathrm{m} < \lambda < 10\ \mu\mathrm{m}$.

The real and imaginary parts of the complex refraction index $m = \sqrt{\varepsilon} = n + ik$ calculated from formula (9.4) with the constants specified above are illustrated in Fig. 9.4(a). The wavelength range in Fig. 9.4(a) is somewhat expanded compared to the range of experimental measurements by Dalzel and Sarofim (from 0.4 to 10 μm) toward shorter wavelengths, so that the high-frequency resonance at $\lambda = 0.26\ \mu\mathrm{m}$ is clearly visible.

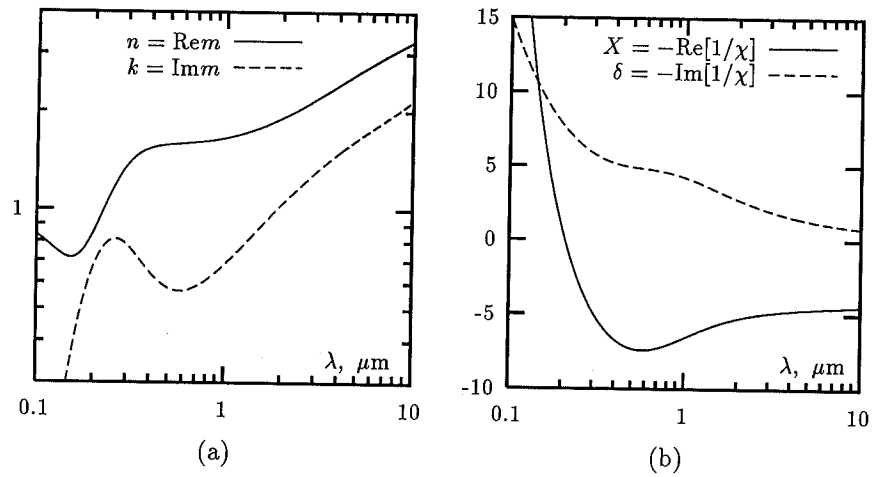

Figure 9.4. (a): Real and imaginary parts of the complex refraction index $m = n + ik$ of carbon calculated from the data of Dalzell and Sarofim [26]. (b): Spectral dependence of the parameters X and δ defined by $1/\chi = -(X + i\delta), \chi = (3/4\pi)(\varepsilon - 1)/(\varepsilon + 2)$.

Analogous three-electron dispersion formulas were used by Habib and Vervisch [28] to describe optical constants of smoke at the flame temperatures. The temperature dependence is mainly governed by the temperature dependence of the conduction electron relaxation constant: $\gamma_c \propto T^{1/2}$ (Lee and Tien [29]). Another issue discussed in the literature is the dependence of the free-electron concentration on the H/C ratio of the fuel [26,28,29].

We use formula (9.4) with the values of constants specified above in all our numerical examples.

In Fig. 9.4(b) we also show the spectral dependence of two important optical parameters, X and δ, which were originally introduced in [30,31].[2] They are defined as $X = -\mathrm{Re}[1/\chi]$, $\delta = -\mathrm{Im}[1/\chi]$, where $\chi = (3/4\pi)(\varepsilon - 1)/(\varepsilon + 2)$. The physical meaning of these parameters is that X is the generalized detuning from the resonance and δ which is the generalized absorption strength. As we will see below, analysis of the spectral dependence of these variables can be useful even when the number of optical resonances is > 1 (at least three in the case of black carbon) and the spectral dependence of ε is more complicated than in the simple Drude model with one optically active electron. Note that X and δ, as defined above, are dimensionless and independent of the sample geometry.

9.4. OPTICAL PROPERTIES OF SMOKE

In this section, we review some of the theoretical and numerical approaches to the calculation of optical characteristics of smoke clusters. In particular, we will discuss optical cross-sections of linear scattering, absorption, and extinction. A special emphasis will be made on the extinction, and numerical examples in this section will be restricted to illustration of the extinction cross-section. A review of the structure factor and scattering in the Born approximation can be found in Chapter 10.

[2]The parameters X and δ used in [30,31] differ from the dimensionless parameters defined below by a multiplicative factor $\pi l^3/6$, which has the dimensionality of length cubed.

9.4.1. Basic Equations

A very convenient starting point for solving the problem of the linear interaction of EM waves with smoke clusters is the Lippman–Schwinger formulation or, more specifically, the Maxwell equations in the integral form, written for the polarization function $\mathbf{P}(\mathbf{r})$ inside the soot material:

$$\mathbf{P}(\mathbf{r}) = \chi\left[\mathbf{E}_{\mathrm{inc}}(\mathbf{r}) + \sum_{i=1}^{N}\int_{V_i} \boldsymbol{G}_R(\mathbf{r}-\mathbf{r}')\mathbf{P}(\mathbf{r}')d^3r'\right] \qquad \mathbf{r} \in V_k \tag{9.5}$$

$$\chi = (3/4\pi)[(\varepsilon - 1)/(\varepsilon + 2)] \tag{9.6}$$

In the next few paragraphs, we explain the notations used in (9.5) and their physical meaning.

First, since we are considering only the linear interaction between the EM fields and matter, Eq. (9.5) is written in the frequency domain for just one (but yet unspecified) value of the frequency ω. The time-dependence factor, $e^{-i\omega t}$, is common to all time-varying quantities and will be omitted everywhere below.

In principle, the incident field $\mathbf{E}_{\mathrm{inc}}$ can be arbitrary as long as it satisfies the free-space Maxwell equations. In most practical cases, the curvature of the wave front of the incident radiation is much larger than the characteristic system size, and it is sufficient to consider incident plane waves of the form

$$\mathbf{E}_{\mathrm{inc}}(\mathbf{r}) = \mathbf{E}_0 \exp(i\mathbf{k}\cdot\mathbf{r}) \tag{9.7}$$

where $k = \omega/c$ is the free-space wavenumber. In this section, we will consider only plane incident waves. However, in Section 9.6 the smoke aggregates will be placed inside water microdroplets and the incident field will be replaced by vector spherical harmonics.

Next, $\boldsymbol{G}_R(\mathbf{r})$ is the *regular* part of the free-space Green's function for the vector wave equation. If there is a point dipole $\mathbf{d}$ at the origin, the electric field at a point $\mathbf{r} \neq 0$ is given by $\mathbf{E}(\mathbf{r}) = \boldsymbol{G}_R(\mathbf{r})\mathbf{d}$. Green's function is a tensor (dyadic) because it transforms one vector into another, which is, in general, not collinear with the first one. The complete Green's function $\boldsymbol{G}(\mathbf{r})$ contains both *regular* and *singular* parts:

$$\boldsymbol{G}(\mathbf{r}) = \boldsymbol{G}_R(\mathbf{r}) - \frac{4\pi}{3}\,\delta(\mathbf{r})\boldsymbol{I} \tag{9.8}$$

where $\boldsymbol{I}$ is the unity tensor and $\delta(\mathbf{r})$ the delta function. The coordinate representation of $\boldsymbol{G}_R(\mathbf{r})$ is given by

$$(G_R(\mathbf{r}))_{\alpha\beta} = k^3[A(kr)\delta_{\alpha\beta} + B(kr)r_\alpha r_\beta/r^2] \tag{9.9}$$

$$A(x) = [x^{-1} + ix^{-2} - x^{-3}]\exp(ix) \tag{9.10}$$

$$B(x) = [-x^{-1} - 3ix^{-2} + 3x^{-3}]\exp(ix) \tag{9.11}$$

where the Greek indexes denote the Cartesian components and $\delta_{\alpha\beta}$ is the Kronecker delta symbol. However, calculation of spatial integrals that arise in the perturbation expansion considered in Section 9.4.2 is much easier with the use of the following representation of the *complete* Green's function:

$$\boldsymbol{G}(\mathbf{r}) = \left(\boldsymbol{I} + \frac{1}{k^2}\nabla\nabla\right)g(\mathbf{r}) \tag{9.12}$$

$$g(\mathbf{r}) = \frac{k^2 e^{ikr}}{r} \tag{9.13}$$

where $g(\mathbf{r})$ is the scalar Green's function. The notation $\nabla\nabla$ can be understood as $\nabla\nabla\mathbf{F} = \nabla(\nabla\cdot\mathbf{F})$.

The integral in (9.5) is taken over the region occupied by the soot material, which is composed from many spherical regions denoted by V_i $(i = 1, \ldots, N)$. We will also denote by V_{tot} the space region occupied by all monomers, that is, $V_{\text{tot}} = V_1 \cup V_2 \cup \ldots \cup V_N$. The center of each spherical region is located at the point $\mathbf{r}_i$, and its radius is R_m (same for all monomers). We denote the monomer volume by v $[v = (4\pi/3)R_m^3]$ and the total volume of all monomers by v_{tot} $(v_{\text{tot}} = Nv)$. Thus, the capital letter V will be used to denote the spatial regions, while small v is their volumes. Below, we will sometimes write $\int_{V_{\text{tot}}}$ as a shortcut for $\sum_{i=1}^{N}\int_{V_i}$.

We also assume that $R_m \ll \lambda$ throughout this chapter. This is a fundamental assumption used in all derivations and numerical examples below. Although it is usually quite accurate, the ratio R_m/λ can become large in the visible spectral range for some types of smoke produced by huge fires (in which case the size of primary spheres tends to be larger), and, of course, R_m/λ cannot be considered as small for shorter wavelengths. The influence of the finite monomer size was studied by Mulholland and co-workers [32,33].

Finally, the coupling constant χ (9.6) is, in fact, the dielectric susceptibility of a sphere in the quasistatic limit. However, no quasistatic approximations were made in Eq. (9.5).

The polarization function $\mathbf{P}(\mathbf{r})$ can be used to calculate all optical properties of the smoke clusters. The scattering amplitude $\mathbf{f}(\mathbf{k}')$ is given by

$$\mathbf{f}(\mathbf{k}') = k^2\int_{V_{\text{tot}}}\left\{\mathbf{P}(\mathbf{r}) - \frac{1}{k^2}\,[\mathbf{P}(\mathbf{r})\cdot\mathbf{k}']\mathbf{k}'\right\}\exp(-i\mathbf{k}'\cdot\mathbf{r})d^3r \tag{9.14}$$

with $\mathbf{k}'$ being the scattered wavevector and $\mathbf{k}$ the incident wavevector, where $|\mathbf{k}| = |\mathbf{k}'| = k = \omega/c$.

The differential scattering cross-section is given by

$$\frac{d\sigma_s}{d\Omega} = \frac{|\mathbf{f}(\mathbf{k}')|^2}{|\mathbf{E}_0|^2} \tag{9.15}$$

and the integral extinction, scattering, and absorption cross-sections, σ_e, σ_s, and σ_a respectively, can be found from the optical theorem:

$$\sigma_e = \frac{4\pi\text{Im}[\mathbf{f}(\mathbf{k})\cdot\mathbf{E}_0^*]}{k|\mathbf{E}_0|^2} \tag{9.16}$$

$$\sigma_s = \frac{1}{|\mathbf{E}_0|^2}\int|\mathbf{f}(\mathbf{k}')|^2 d\Omega \tag{9.17}$$

$$\sigma_a = \sigma_e - \sigma_s \tag{9.18}$$

where we have assumed excitation by a plane wave of the form (9.7).

The expression for the extinction cross-section follows readily from (9.16) and (9.14):

$$\sigma_e = \frac{4\pi k}{|\mathbf{E}_0|^2}\,\text{Im}\int_{V_{\text{tot}}}\mathbf{P}(\mathbf{r})\cdot\mathbf{E}_{\text{inc}}^*(\mathbf{r})d^3r \tag{9.19}$$

The expressions for the integral scattering and absorption cross-sections contai double volume integration, since σ_s is quadratic in $\mathbf{f}$. However, the angular integra tion in (9.17) and one of the volume integrals can be calculated in the most gener form with the use of the main equation (9.5) [34,35], which leads to expressions f the integral cross-sections that contain only one volume integration. The result f the absorption has a more compact form:

$$\sigma_a = \frac{4\pi k\delta}{|\mathbf{E}_0|^2}\int_{V_{\text{tot}}}\mathbf{P}^*(\mathbf{r})\cdot\mathbf{P}(\mathbf{r})d^3r \tag{9.20}$$

where the parameter $\delta = -\text{Im}[1/\chi]$ was introduced in Section 9.3. The integr scattering cross-section can be found as the difference between (9.19) and (9.20)

The above formulas take an elegant form if we introduce operator notations. Firs we notice that the integral transformation on the right-hand side (rhs) of Eq. (9.5) h the form of a linear integral operator acting on what can be viewed as an element an infinite-dimensional Hilbert space $L_2(V_{\text{tot}})$ of vector functions that are squa integrable in V_{tot}. Thus, we can introduce a linear operator W that acts on an arbitra element $|f\rangle$ of $L_2(V_{\text{tot}})$ according to the rule

$$W|f\rangle \to \int_{V_{\text{tot}}}\boldsymbol{G}_R(\mathbf{r}-\mathbf{r}')\mathbf{f}(\mathbf{r}')d^3r' \qquad \mathbf{r}\in V_{\text{tot}} \tag{9.2}$$

The operator W is an infinite-dimensional symmetrical operator. It is a "mixed" operator in the sense that it is both tensorial and integral. We can easily verify that if $|f\rangle$ is an element of $L_2(V_{\text{tot}})$, then $W|f\rangle$ is also an element of $L_2(V_{\text{tot}})$. Further, we can define a scalar product of two vectors $|f\rangle$ and $|g\rangle$ and a norm in $L_2(V_{\text{tot}})$ as

$$\langle g|f\rangle = \int_{V_{\text{tot}}} \mathbf{g}^*(\mathbf{r}) \cdot \mathbf{f}(\mathbf{r}) d^3r \tag{9.22}$$

$$\|f\| = \sqrt{\langle f|f\rangle} \tag{9.23}$$

respectively. Using the above notations, we can rewrite (9.5) as

$$|P\rangle = \chi[|E_{\text{inc}}\rangle + W|P\rangle] \tag{9.24}$$

where the vector $|P\rangle$ corresponds to the polarization function $\mathbf{P}(\mathbf{r})$ and $|E_{\text{inc}}\rangle$ to the incident field. The expressions for the optical cross-sections take the following forms:

$$\sigma_e = \frac{4\pi k}{|\mathbf{E}_0|^2} \operatorname{Im}\langle E_{\text{inc}}|P\rangle \qquad \sigma_a = \frac{4\pi k\delta}{|\mathbf{E}_0|^2} \langle P|P\rangle \tag{9.25}$$

To conclude this section, we raise the consideration to a slightly higher level of abstraction. The solution to the operator equation (9.24) can be written in symbolic form as

$$|P\rangle = [1/\chi - W]^{-1}|E_{\text{inc}}\rangle \tag{9.26}$$

The operator $R(E) = [E - W]^{-1}$, where E is an arbitrary (complex) scalar is called the *resolvent* of the operator W. The extinction cross-section is given by the diagonal matrix element of the resolvent, $\langle E_{\text{inc}}|R(1/\chi)|E_{\text{inc}}\rangle$.

For an arbitrary Hermitian operator H, the resolvent can be expanded in terms of the eigenvectors of H as

$$R(E) = \frac{1}{E - H} = \sum_n \frac{|n\rangle\langle n|}{E - E_n} \tag{9.27}$$

where $|n\rangle$ and E_n are the eigenvectors and eigenvalues of H. However, W is not Hermitian but *complex and symmetrical*. The symmetry of W should be understood as the following property of the kernel $\boldsymbol{G}_R$:

$$\boldsymbol{G}_R(\mathbf{r}) = \boldsymbol{G}_R(-\mathbf{r}), \ (G_R(\mathbf{r}))_{\alpha\beta} = (G_R(\mathbf{r}))_{\beta\alpha} \tag{9.28}$$

These two equalities provide that, for two arbitrary elements of $L_2(V_{\text{tot}})$, $|f\rangle$ and $|g\rangle$,

$$\langle f^*|W|g\rangle = \langle g^*|W|f\rangle \tag{9.29}$$

where the asterisk denotes the complex conjugation (c.c.) of the corresponding function.[3] Equation (9.29) can be viewed as a generalized symmetry condition for W. It can be used to prove that if $|f\rangle$ and $|g\rangle$ are two different (linear independent) eigenvectors of W, they obey $\langle \mathrm{f}^*|\mathrm{g}\rangle = 0$ [34], which is an analog of the orthogonality condition for eigenfunctions of Hermitian operators, $\langle f|g\rangle = 0$. This property, in turn, can be used to write an analog of expansion (9.27) for the non-Hermitian operator W:

$$R(E) = \frac{1}{E - W} = \sum_n \frac{|n\rangle\langle n^*|}{\langle n^*|n\rangle[E - w_n]} \tag{9.30}$$

Analogously to the notations of Eq. (9.27), we denote the eigenvectors and eigenvalues of W by $|n\rangle$ and w_n. However, now w_n is, generally, a complex number, as well as the factor $\langle n^*|n\rangle$ in the denominator of (9.30). We emphasize that $\langle n^*|n\rangle \neq \langle n|n\rangle$. The latter value is equal to unity for normalized eigenvectors, while the former is a complex number.

Now, we recall that the generic variable E has to be substituted by $1/\chi$ in (9.30). This fact and the structure of Eq. (9.30) emphasize the importance of the parameters X and δ introduced at the end of Section 9.3. According to the definition, $1/\chi = -(X + i\delta)$. If the interaction between monomers is turned off, for example, by disaggregating a smoke cluster and moving the monomers far from each other, all the eigenvalues w_n turn to zero. Then, X plays the role of the generalized detuning from the resonance of an isolated (noninteracting) monomer, while δ is the energy loss parameter (again, in the absence of interaction). In the presence of interaction, the eigenvalues w_n become nonzero. The real parts of w_n's describe frequency shifts of collective resonances, while the imaginary parts can change the collective radiative losses due to constructive or destructive interference.

In the quasistatic approximation, when the system size is much smaller than the wavelength, the operator W becomes Hermitian, and all w_n's are real and independent of the optical frequency [31]. The only source of the spectral dependence of the solution is in this case the spectral dependence of X and δ on λ.

9.4.2. Perturbative Methods

It is convenient to build the perturbation expansions of the optical cross-sections starting from the operator form (9.24) of the integral Maxwell equations. The Born expansion for the polarization function $|P\rangle$ is obtained by iterating (9.24):

$$|P\rangle = \chi \sum_{k=0}^{\infty} (\chi W)^k |E_{\text{inc}}\rangle \tag{9.31}$$

[3] In our notations, the symbol $\langle f|$ stands for the c.c. of the function $\mathbf{f}$, and hence, $\langle f^*|$ is, in fact, the function $\mathbf{f}$ itself. This system of notations may seem to be artificial, but we have decided to follow the standard Dirac notations, though they are more appropriate for Hermitian operators, while the operator W is not Hermitian.

The corresponding expansion for the extinction cross-section follows from (9.25) and (9.31):

$$\sigma_e = 4\pi k v_{\text{tot}} \operatorname{Im}\left[\chi \sum_{k=0}^{\infty} B_k \chi^k\right] \qquad B_k \equiv \frac{\langle E_{\text{inc}}|W^k|E_{\text{inc}}\rangle}{\langle E_{\text{inc}}|E_{\text{inc}}\rangle} \tag{9.32}$$

where we have taken into account that $\langle E_{\text{inc}}|E_{\text{inc}}\rangle = v_{\text{tot}}|\mathbf{E}_0|^2$. Because W is an integral operator [see (9.21)], a calculation of the coefficients B_k requires a calculation of $k+1$ volume integrals over V_{tot}. The approximation in which only the first nonzero term in (9.32) is left is often called the first Born approximation (the corresponding coefficient is B_0 in our notations). Multiple scattering is completely neglected in this approximation. In the next order (second Born approximation), the coefficient B_1 is retained. Physically, this is equivalent to taking into account double scattering. The convergence condition for the Born expansion is $\max[|\chi w_n|] < 1$.

One can improve the convergence of the perturbation expansion for σ_e by adopting a more sophisticated approach. According to (9.25), (9.26), $\sigma_e \propto \operatorname{Im}\langle E_{\text{inc}}|R(1/\chi)|E_{\text{inc}}\rangle$, where $R(E) = [E - W]^{-1}$. To obtain an expansion of this matrix element of the resolvent, we build an infinite sequence of vectors $|P_k\rangle$ and complex numbers Q_k such that († stands for Hermitian conjugation)

$$W^\dagger|P_k\rangle = Q_{k+1}^*|E_{\text{inc}}\rangle + |P_{k+1}\rangle, \quad k = 0,\ 1,\ 2,\ \ldots \tag{9.33}$$

$$\langle P_k|E_{\text{inc}}\rangle = 0, \forall k > 0 \tag{9.34}$$

$$|P_0\rangle = |E_{\text{inc}}\rangle \tag{9.35}$$

It is straightforward to show that recursion (9.33) defines a unique set of $|P_k\rangle$ and Q_k and

$$|P_k\rangle = (TW^\dagger)^k|E_{\text{inc}}\rangle \qquad k = 0,\ 1,\ 2,\ \ldots \tag{9.36}$$

$$Q_k = \frac{\langle E_{\text{inc}}|W(TW)^{k-1}|E_{\text{inc}}\rangle}{\langle E_{\text{inc}}|E_{\text{inc}}\rangle} \qquad k = 1,\ 2,\ 3,\ \ldots \tag{9.37}$$

$$T \equiv 1 - \frac{|E_{\text{inc}}\rangle\langle E_{\text{inc}}|}{\langle E_{\text{inc}}|E_{\text{inc}}\rangle} \tag{9.38}$$

Here, T is the projection operator with respect to the vector $|E_{\text{inc}}\rangle$. Note that the vectors $|P_k\rangle$ are, in general, not normalized or mutually orthogonal.

Next, we define a vector $|\psi\rangle \equiv [1/\chi - W]^{-1}|E_{\text{inc}}\rangle$, so that $\langle E_{\text{inc}}|R(1/\chi)|E_{\text{inc}}\rangle = \langle E_{\text{inc}}|\psi\rangle$, and notice that $\langle E_{\text{inc}}|\psi\rangle$ must satisfy the equation

$$\langle E_{\text{inc}}|\psi\rangle = \chi[\langle E_{\text{inc}}|E_{\text{inc}}\rangle + \langle E_{\text{inc}}|W|\psi\rangle] \tag{9.39}$$

It also follows from the definition of $|\psi\rangle$ that

$$\langle P_k|W|\psi\rangle = Q_{k+1}\langle E_{\text{inc}}|\psi\rangle + \chi\langle P_{k+1}|W|\psi\rangle, \ k \geq 0 \tag{9.40}$$

If we act repeatedly n times by the operator W to the left in Eq. (9.39) and use the recursion (9.40), we obtain

$$\langle E_{\text{inc}}|\psi\rangle = \chi[\langle E_{\text{inc}}|E_{\text{inc}}\rangle + (Q_1 + Q_2\chi + Q_3\chi^2 + \cdots + Q_n\chi^{n-1})\langle E_{\text{inc}}|\psi\rangle + \chi^n\langle P_n|W|\psi\rangle] \tag{9.41}$$

Equation (9.41) can be rewritten as

$$\langle E_{\text{inc}}|R(1/\chi)|E_{\text{inc}}\rangle = \langle E_{\text{inc}}|\psi\rangle = \frac{\chi\langle E_{\text{inc}}|E_{\text{inc}}\rangle}{1 - \sum_{k=1}^{n} Q_k\chi^k} + \xi_n \tag{9.42}$$

The residual term, ξ_n, still depends on the unknown vector $|\psi\rangle$ and is given by

$$\xi_n = \chi^n\langle P_n|\psi\rangle\left[1 - \sum_{k=1}^{n} Q_k\chi^k\right]^{-1} \tag{9.43}$$

If we neglect ξ_n, we can write the expansion for the extinction cross-section:

$$\sigma_e = 4\pi k v_{\text{tot}} \operatorname{Im}\left[\frac{\langle E_{\text{inc}}|R(E)|E_{\text{inc}}\rangle}{\langle E_{\text{inc}}|E_{\text{inc}}\rangle}\right] = 4\pi k v_{\text{tot}} \operatorname{Im}\left[\frac{\chi}{1 - \sum_{k=1}^{\infty} Q_k\chi^k}\right] \tag{9.44}$$

Equivalently, this can be rewritten as

$$\sigma_e = 4\pi k v_{\text{tot}} \operatorname{Im}\left[\frac{1}{1/\chi - Q_1 - \Sigma(\chi)}\right] \tag{9.45}$$

where the self-energy $\Sigma(\chi)$ is given by $\Sigma(\chi) = \sum_{k=1}^{\infty} Q_{k+1}\chi^k$. The expansion (9.45) has the form of the Dyson equation. In the first order, by neglecting the self-energy, we recover the result of the mean-field approximation, which was introduced by Berry and Percival [20] for the problem of scattering of light by fractal smoke clusters (the constant Q_1 in (9.45) is analogous to the constant P in [20]). In fact, the mean-field result serves as the first-order approximation for the above expansion.

The expansion coefficients Q_k can be easily expressed in terms of the corresponding coefficients for the Born expansion, B_k. For the first few terms, $Q_1 = B_1$, $Q_2 = B_2 - B_1^2$, $Q_3 = B_3 - 2B_1B_2 + B_1^3$. Therefore, in order to build the expansion (9.45), it is sufficient to calculate the volume integrals involved in the calculation of the B_k's.

It is instructive to compare the expansion (9.44) with the Born expansion. One can show (the details of the derivation are omitted) that the Taylor expansion of (9.44) with respect to powers of χ, where only the n first Q_k's are left in the denominator, exactly coincides with the Born expansion (9.32) up to the order $k = n$ in χ. For $k > n$, the absolute value of the difference between the coefficients in these two expansions is not greater than the absolute values of the corresponding

coefficients B_k. For example, in the $n = 2$ case, the difference in the third-order coefficients is $B_3 - 2Q_1Q_2 - Q_3^3 = \langle E_{\text{inc}}|W|E_{\text{inc}}\rangle^3$, and $|\langle E_{\text{inc}}|W|E_{\text{inc}}\rangle|^3 \le |B_3| = |\langle E_{\text{inc}}|W^3|E_{\text{inc}}\rangle|$ (generalized Hölder inequality). Practically, this means that (1) if the expansion (9.32) converges, the expansion (9.44) also converges and (2) the convergence of (9.44) is at least as fast as that of (9.32). Even in the first order, the expansion (9.44) contains infinite orders of multiple scattering, which is known to be true for the mean-field approximation [20].

Now, we turn our attention to the calculation of the coefficients B_k. The first coefficient is trivial, $B_0 = 1$. Next, we recall that W is an integral operator defined by (9.21) and write B_1 as

$$B_1 = \frac{\langle E_{\text{inc}}|W|E_{\text{inc}}\rangle}{v_{\text{tot}}|\mathbf{E}_0|^2} \tag{9.46}$$

$$\langle E_{\text{inc}}|W|E_{\text{inc}}\rangle = \sum_{i,j=1}^{N}\int_{V_i} d^3r \int_{V_j} d^3r'[\mathbf{E}^*_{\text{inc}}(\mathbf{r})\cdot \boldsymbol{G}_R(\mathbf{r}-\mathbf{r}')\mathbf{E}_{\text{inc}}(\mathbf{r}')] \tag{9.47}$$

By using the fundamental assumption of small primary particles $kR_m \ll 1$ (R_m is the radius of the spherical volumes V_i, V_j) and by using Eq. (9.7), we replace $\mathbf{E}_{\text{inc}}(\mathbf{r}')$ by $\mathbf{E}_0 \exp(i\mathbf{k}\cdot\mathbf{r}_j)$ and $\mathbf{E}^*_{\text{inc}}(\mathbf{r})$ — by $\mathbf{E}_0 \exp(-i\mathbf{k}\cdot\mathbf{r}_i)$ in the above integral, and group the terms with $i = j$ together to obtain

$$\begin{aligned}\langle E_{\text{inc}}|W|E_{\text{inc}}\rangle = &\sum_i \int_{V_i} d^3r \int_{V_i} d^3r'[\mathbf{E}_0^*\cdot \boldsymbol{G}_R(\mathbf{r}-\mathbf{r}')\mathbf{E}_0] \\ &+ \sum_{i\neq j} e^{i\mathbf{k}\cdot(\mathbf{r}_j-\mathbf{r}_i)}\int_{V_i} d^3r \int_{V_j} d^3r'[\mathbf{E}_0^*\cdot \boldsymbol{G}_R(\mathbf{r}-\mathbf{r}')\mathbf{E}_0]\end{aligned} \tag{9.48}$$

The double integral over the same volume V_i in the first term of (9.48) turns to zero in the limit $R_m \ll \lambda$. This can be easily illustrated by considering Eq. (9.5) for a single sphere case ($N = 1$) and observing that in this limit $\mathbf{P} = \chi\mathbf{E}_0 = \text{const}$ inside the sphere; hence, the integral on the rhs of (9.5) must go to zero. The integral over the different volumes V_i and V_j can be easily evaluated using (9.12), (9.13), and the spherical harmonic expansion of $g(\mathbf{r}-\mathbf{r}')$ [36]:

$$g(\mathbf{r}-\mathbf{r}') = 4\pi ik^3 \sum_{l=0}^{\infty}\sum_{m=-l}^{l} j_l(kr_<)h_l^{(1)}(kr_>)Y^*_{lm}(\Omega_{\mathbf{r}'})Y_{lm}(\Omega_{\mathbf{r}}) \tag{9.49}$$

where $j_l(x)$, $h_l^{(1)}(x)$ are the spherical Bessel and Hankel functions, $r_< = \min(r,\ r')$, $r_> = \max(r,\ r')$, and $Y_{lm}(\Omega_{\mathbf{r}})$ are spherical harmonics. By choosing the origin at the center of the volume V_j, we find that $r_> = r$, $r_< = r'$, and

$$\int_{V_j} g(\mathbf{r}-\mathbf{r}')d^3r' = 4\pi ik^3 \sum_{l=0}^{\infty}\sum_{m=-l}^{l} h_l^{(1)}(kr)Y_{lm}(\Omega_{\mathbf{r}})\int_0^{R_m} j_l(kr')(r')^2dr' \int Y^*_{lm}(\Omega_{\mathbf{r}'})d\Omega_{\mathbf{r}'} \tag{9.50}$$

If we take account of the fact that $\int Y^*_{lm}(\Omega_{\mathbf{r}'})d\Omega_{\mathbf{r}'} = \sqrt{4\pi}\delta_{l0}\delta_{m0}$, this is simplified to

$$\int_{V_j} g(\mathbf{r}-\mathbf{r}')d^3r' = 4\pi ih_0^{(1)}(kr)\int_0^{kR_m} j_0(x)x^2dx = v\beta(kR_m)g(\mathbf{r}) \tag{9.51}$$

$$\beta(x) = 3j_1(x)/x = 3(\sin x - x\cos x)/x^3 \tag{9.52}$$

The Taylor expansion of $\beta(x)$ near $x = 0$ is $\beta(x) = 1 - x^2/10 + \ldots$. Since we already neglected the phase dependence of the incident field over the volume of integration, keeping the terms of the order of x^2 amounts to excessive precision. Therefore, we set $\beta = 1$. The integration was performed in a reference frame, where $\mathbf{r}_j = 0$. In a general reference frame, one has

$$\int_{V_j} g(\mathbf{r}-\mathbf{r}')d^3r' = vg(\mathbf{r}-\mathbf{r}_j) \qquad \mathbf{r}\notin V_j \tag{9.53}$$

Consequently, for the integral of the tensor Green's function $\boldsymbol{G}_R$ one has

$$\int_{V_j} \boldsymbol{G}_R(\mathbf{r}-\mathbf{r}')d^3r' = v\left(\boldsymbol{I} + \frac{1}{k^2}\hat{\nabla}_{\mathbf{r}}\hat{\nabla}_{\mathbf{r}}\right)\int_{V_j} g(\mathbf{r}-\mathbf{r}')d^3r' = v\boldsymbol{G}_R(\mathbf{r}-\mathbf{r}_j), \qquad \mathbf{r}\notin V_j \tag{9.54}$$

Repeating analogous integration over the variable $\mathbf{r}\in V_i$, we obtain

$$\int_{V_i} d^3r \int_{V_j} d^3r'\boldsymbol{G}_R(\mathbf{r}-\mathbf{r}') = v^2\boldsymbol{G}_R(\mathbf{r}_i-\mathbf{r}_j) \qquad i\neq j \tag{9.55}$$

The above result seems to be obvious for two spheres that are separated by a distance much larger than their radii, but much less so for two touching spheres. However, it is exact in the limit $kR_m \to 0$. The physical interpretation of Eq. (9.55) is that in this particular order of the perturbation expansion each sphere can be adequately represented by a point dipole moment located in its center. In other words, the integral equations can be replaced by a set of discrete equations with respect to the dipole moments of the monomers, which constitutes the essence of the dipole approximation. It might seem that the dipole approximation must work simply because kR_m is small. However, this is known not to be the case for interacting spheres in close vicinity of each other (we will return to this in Section 9.4.3). In fact, the dipole approximation breaks down in the next order of the perturbation expansion.

Returning to calculation of B_1, we find

$$B_1 = \frac{v}{N|\mathbf{E}_0|^2}\sum_{i\neq j} e^{-i\mathbf{k}\cdot\mathbf{r}_{ij}}\mathbf{E}_0^*\cdot\boldsymbol{G}_R(\mathbf{r}_{ij})\mathbf{E}_0 \qquad \mathbf{r}_{ij} = \mathbf{r}_i - \mathbf{r}_j \tag{9.56}$$

Now, we proceed with statistical averaging of (9.56). This averaging can be introduced in two different ways. First, if a soot cluster is large enough, the probability distribution for the absolute values r_{ij} must be given by the pair correlation function $p(r_{ij})$ that was discussed in Section 9.2, while all the spatial orientations of $\mathbf{r}_{ij}$ are equiprobable (clusters are spherically symmetrical on average). This can be called self-averaging. The other approach is ensemble averaging over a distribution of different realizations of random clusters. The orientational averaging can be easily carried out in a spherical system of coordinates where the direction of vector $\mathbf{k}$ coincides with the z-axis and the direction of $\mathbf{E}_0$ (assuming linear polarization) with the x-axis. Then, using the tensor structure of $\boldsymbol{G}_R$ (9.9–9.11), we obtain

$$B_1 = k^3 v (N-1)\langle e^{-ikr_{ij}\cos\theta}[A(kr_{ij}) + B(kr_{ij})\sin^2\theta\cos^2\phi]\rangle \tag{9.57}$$

where we have taken into account that the total number of terms in the sum (9.56) is $N(N-1)$ and $\langle\cdots\rangle$ stands for statistical averaging. Orientational averaging is easily achieved by integrating (9.57) over $\sin\theta\, d\theta\, d\phi/(4\pi)$. The radial averaging is done with the use of the correlation function $p(r)$ (9.1) which is, by definition, the probability density to find a distinct pair of monomers in a cluster separated by the distance r. If we use the functional form (9.1) for $p(r)$, we arrive at

$$B_1 = \frac{\pi a}{6}(kl)^{3-D}\int_0^\infty x^{D-1} f\left(\frac{x}{kR_g}\right)F(x)dx \tag{9.58}$$

where $a \approx 4$ is the numerical constant, $f(x)$ is the cutoff function discussed in Section 9.2, we have used $v = (\pi/6)l^3$, and $F(x)$ is the result of angular integration of (9.57):

$$F(x) = \frac{\sin x}{x}A(x) - \left(\frac{\cos x}{x^2} - \frac{\sin x}{x^3}\right)B(x) \tag{9.59}$$

and $A(x)$, $B(x)$ are defined by (9.10) and (9.11). The power series expansion of $F(x)$ near $x = 0$ is $F(x) = (11/15)x^{-1} + 2i/3 - (46/105)x - (2i/9)x^2 + O[x^3]$. Therefore, the radial integral in (9.58) converges at the lower limit for $D > 1$, that is, for any physically reasonable fractal dimension. As was discussed in Section 9.2, this fact justifies the extension of the region of applicability of the scaling formula (9.1) to $r = 0$.

Convergence at $r = \infty$ is guaranteed by the cutoff function $f(x)$. However, for $D < 2$, (9.58) converges at the upper limit of integration even if we set $f(x/kR_g) = 1$. Therefore, for large clusters with $kR_g \gg 1$, the integral (9.58) converges while the cutoff function f is still close to unity. This means that for sufficiently large clusters with $D < 2$ (which is usually the case), the particular form of the cutoff function is not important, and we can calculate the integral (9.58) analytically [20]. The final

result of integration is

$$B_1 = \frac{\pi a}{24}(2kl)^{3-D}\exp\left[\frac{i\pi(D+1)}{2}\right]K(D) \qquad 1 < D < 2,\quad kR_g \gg 1 \tag{9.60}$$

$$K(D) = \frac{\Gamma(D)}{(D-1)(2-D)(3-D)}\left[\frac{4(5D-18)}{(4-D)(6-D)} + D + 1\right] \tag{9.61}$$

where $\Gamma(x)$ is the gamma function.

Note that the function $K(D)$ in (9.61) diverges as D approaches 2. This result indicates that the perturbation expansion for large clusters becomes less accurate as D approaches 2. However, there is no real divergence even for $D > 2$ because of the cutoff function $f(x/kR_g)$, which was set to unity for the derivation of (9.60). Therefore, the result (9.60) should be used with caution. In particular, progressively larger values of kR_g are required for convergence of the integral when D approaches 2. In general, when kR_g is not sufficiently large, or $D > 2$, the value of B_1 depends on the exact form of $f(x)$ and on the gyration radius of the cluster, R_g. The dependence of the integral of the type (9.58) on D for the simple exponential cutoff was considered by Berry and Percival [20] and by Shalaev et al. [37].

The result (9.60) was obtained in the "intermediate" wavelength limit $R_m \ll \lambda \ll R_g$. It is also possible to calculate B_1 in the long-wavelength limit $R_m \ll R_g \ll \lambda$ (the quasistatic approximation). This can be easily done by observing that, when $kR_g \gg 1$, the integral (9.58) converges for small values of x. Therefore, we can keep only the first two terms in the power series expansion of $F(x)$ near $x = 0$, which is necessary to calculate both the real and imaginary parts of B_1: $F(x) \approx (11/15)x^{-1} + 2i/3$. By substituting this expression into (9.58), and by using (9.2), we obtain

$$B_1 = ab^D k^3 v_{\text{tot}}\left[\frac{11}{15kR_g}\int_0^\infty x^{D-2}f(x)dx + \frac{2i}{3}\int_0^\infty x^{D-1}f(x)dx\right] \tag{9.62}$$

In expression (9.62), a, b are the numerical coefficients [see formulas (9.1) and (9.2) for the definitions]. As was mentioned in Section 9.2, the dimensionless combination ab^D is $\simeq 1.6$ for cluster–cluster aggregates. The integrals on the rhs of (9.62) are simple numbers, and can be evaluated numerically given a specific form of the cutoff function $f(x)$. If $f(x)$ is given by the generalized exponential formula with constants described in the caption of Fig. 9.2, the integrals are $\simeq 1.6$ and 1.2, respectively. As can be seen from (9.62), the coefficient B_1 becomes purely real in the limit $\lambda \to \infty$.

As was mentioned above, the calculation of higher coefficients B_k cannot be performed in the "dipole approximation". In practice, this means that the chain integrals of the kind

$$\int_{V_{i_1}} d^3r_1 \int_{V_{i_2}} d^3r_2 \cdots \int_{V_{i_n}} d^3r_n \boldsymbol{G}_R(\mathbf{r}_1 - \mathbf{r}_2)\boldsymbol{G}_R(\mathbf{r}_2 - \mathbf{r}_3)\cdots\boldsymbol{G}_R(\mathbf{r}_{n-1} - \mathbf{r}_n)$$

cannot be represented as

$$v^n \boldsymbol{G}_R(\mathbf{r}_{i_1} - \mathbf{r}_{i_2})\boldsymbol{G}_R(\mathbf{r}_{i_2} - \mathbf{r}_{i_3}) \cdots \boldsymbol{G}_R(\mathbf{r}_{i_{n-1}} - \mathbf{r}_{i_n})$$

Generally, this simple integration rule can only be applied to the "end of chain" integration variables ($\mathbf{r}_1$ and $\mathbf{r}_n$ in the above example). In the case of the double scattering coefficient B_1, both integration variables are, effectively, "end of chain," and the dipole approximation works. The integration variable $\mathbf{r}_2$ in the above example is "middle of the chain," in other words, it appears in two Green's functions instead of one. Therefore, the integration over $\mathbf{r}_2$ cannot be so easily performed.

9.4.3. Nonperturbative Methods

As we saw in Section 9.4.2, the dipole approximation is accurate up to the second order of the Born expansion. This indicates that when the interaction is weak, both the perturbation expansion and dipole approximation become accurate. Of course, it is also possible to formulate the dipole approximation nonperturbatively, which is done below.

In the dipole approximation, each monomer in a cluster is considered to be a point dipole with polarizability α, located at the point $\mathbf{r}_i$ (at the center of the respective spherical monomer). The dipole moment of the ith monomer, $\mathbf{d}_i = \int_{V_i} \mathbf{P}(\mathbf{r})d^3r$, is proportional to the external electric field at the point $\mathbf{r}_i$, which is a superposition of the incident field and all the secondary fields scattered by other dipoles. Therefore, the dipole moments of the monomers are coupled to the incident field and to each other as described by the coupled dipole equation (CDE):

$$\mathbf{d}_i = \alpha\left[\mathbf{E}_{\text{inc}}(\mathbf{r}_i) + \sum_{j\neq i}^{N} \boldsymbol{G}_R(\mathbf{r}_i - \mathbf{r}_j)\mathbf{d}_j\right] \tag{9.63}$$

which is simply a discrete version of the integral equation (9.5). It was introduced in the context of the discrete dipole approximation by Purcell and Pennypacker [38], and for fractal clusters by Markel et al. [30,31].[4] The CDE is a system of $3N$ linear equations that can be solved to find the dipole moments $\mathbf{d}_i$. All the optical cross sections can be found in complete analogy with (9.14)–(9.20):

$$\mathbf{f}(\mathbf{k}') = k^2 \sum_{i=1}^{N} \left[\mathbf{d}_i - (\mathbf{d}_i \cdot \mathbf{k}')\mathbf{k}'/k^2\right] \exp(-i\mathbf{k}' \cdot \mathbf{r}_i) \tag{9.64}$$

$$\sigma_e = \frac{4\pi k}{|\mathbf{E}_0|^2} \operatorname{Im} \sum_{i=1}^{N} \mathbf{d}_i \cdot \mathbf{E}^*_{\text{inc}}(\mathbf{r}_i) \tag{9.65}$$

[4]The discrete dipole approximation, although leading to similar equations, is used to solve a problem essentially different from the one described in this chapter. For more references, see [39,40].

$$\sigma_a = \frac{4\pi k y_a}{|\mathbf{E}_0|^2} \sum_{i=1}^{N} |\mathbf{d}_i|^2 \tag{9.66}$$

$$y_a \equiv -\operatorname{Im}\left(\frac{1}{\alpha}\right) - \frac{2k^3}{3} = \delta/v \geq 0 \tag{9.67}$$

The last formula (9.67) needs an explanation. The definition of the absorption parameter y_a in (9.66) follows from rigorous integration of the scattering amplitude (9.64) [34]. It must be nonnegatively defined for any physically reasonable polarizability α [41]. However, if we use the usual relation between the polarizability α and susceptibility χ, $\alpha = v\chi$, this condition [as well as the second equality in (9.67)] can be violated for purely real values of ε when χ is also real. As was shown by Draine [39], the above relation between α and χ should be modified to take into account radiative reaction. The corrected formula is $1/\alpha = 1/v\chi - i2k^3/3$, which, taking into account $\delta = -\operatorname{Im}[1/\chi]$, immediately leads to the second equality in (9.67). For strongly absorbing carbon, the radiative corrections are negligibly small.

The advantage of the dipole approximation is simplicity: An integral equation is replaced by a finite system of linear equations. However, we already saw that the dipole approximation is not accurate in the third, and all the higher, orders of the perturbation expansion. In fact, the general nonapplicability of the dipole approximation was recognized and verified both theoretically [42,43] and experimentally [44]. A simple physical explanation of why the dipole approximation fails was provided, for example, by Sansonetti and Furdyna [44]. First, in the dipole approximation, the local field acting on a certain dipole is evaluated at the center of the corresponding monomer. However, the field produced by neighboring monomers is highly nonuniform over the volume of the first monomer, and cannot be replaced by a single value. And second, the dipole approximation neglects higher multipole moments of the monomers, which is a good approximation for those monomers which are far away from each other, but not for nearest neighbors. Effectively, by replacing two touching spheres by two point dipoles located at their centers, we underestimate the strength of their interaction.

To overcome the limitations of the dipole approximation, a rigorous numeric approach has been developed by Gerardy and Ausloos [42] (in the long-wavelength limit), Claro [43,45,46] and Claro and co-workers [47,48], Mackowski [49], Mackowski and Mischenko [50], Fuller [51,52], and Xu [53]. The essence of the method is to expand the EM field inside each sphere and the field scattered by each sphere in vector spherical harmonics, and to match the boundary condition on the surfaces of discontinuity. Generally, this method leads to an infinite - dimensional system of linear equations with respect to the expansion coefficients. In order to solve this system, one needs to truncate it by assuming that all the expansion coefficients for spherical harmonics of the order larger than L are zero. Then, the total number of equation scales (for large values of L) as NL^2.

Although a detailed description of the above methods is beyond the scope of this chapter, in Section 9.4.4, we will illustrate with a numerical example an important trend: When the interaction of monomers in a cluster becomes stronger and

perturbation expansion, correspondingly, less accurate (or even diverges), the maximum number L required for attaining accurate results tends to increase. This makes the "coupled multipoles" method computationally applicable only for situations with either a small number of monomers or weak interaction.

To overcome the inadequacy of the dipole approximation and the overwhelming computational complexity of the "coupled multipole" method, we have suggested a phenomenological procedure that can be referred to as the cluster renormalization approach [54,55]. This approach allows one to stay in the frame of the dipole approximation, and is described in detail below. The following two factors are important for understanding the renormalization approach.

First, we note that most calculations employ computer - generated samples. The geometry of these samples does not coincide with that of experimental soot exactly, which is obviously impossible, but rather reproduces certain statistical geometrical properties of real soot. Among such properties are density correlation functions, total volume of the material, and average radius of gyration, R_g. However, such characteristics as the number of monomers in a cluster, N, and monomer radius, R_m, might be considered as *not essential*. It is known, for example, that the real carbon monomers are not actually spherical, and nearest neighbors touch each other at more than just one geometrical point, so that the model of touching spheres is only an idealization. Second, as mentioned above, the dipole approximation in its pure form underestimates the interaction strength. In particular, it predicts the shift of the resonance frequency in small clusters of spheres to be significantly less than is experimentally measured [44]. In order to correct the interaction strength of the dipole approximation, it is tempting to move the monomers closer to each other (of course, this relates to computer-generated samples) by allowing them to intersect geometrically. However, doing this will evidently reduce the overall system size (R_g), which is an essential parameter of the problem. The other possible way to introduce the intersections is to increase the radii of the spheres (R_m) while keeping distance between nearest neighbors (l) unchanged. This will, however, lead to an increase of the total volume of the material. Luckily, for fractal clusters, it is possible to introduce a simultaneous renormalization of the sphere radii (R_m), the total number of monomers (N) and the distance between nearest neighbors (l) in such a way that the overall volume (v_{tot}) and the gyration radius (R_g) are unchanged, and to introduce an arbitrary geometrical intersection of neighboring spheres. The transformation is

$$R'_m = R_m \left(\frac{\xi}{2}\right)^{D/(3-D)} \tag{9.68}$$

$$N' = N \left(\frac{2}{\xi}\right)^{3D/(3-D)} \tag{9.69}$$

$$l' = \xi R'_m \tag{9.70}$$

where ξ is a phenomenological intersection parameter ($1 < \xi \leq 2$, $\xi = 2$ for touching spheres and $\xi < 2$ for geometrically intersecting spheres).

Thus, the main idea of the renormalization approach is to model an ensemble of real clusters with experimental values of R_m and N (and $l = 2R_m$) by a computer-generated "renormalized" ensemble with corresponding parameters R'_m, N', and with the geometrical intersection of neighboring spheres: $l' = \xi R'_m < 2R'_m$. The intersection parameter ξ is phenomenological and must be adjusted. The initial value for ξ can be obtained from the following simple considerations, which can be also used to justify the physical plausibility of the renormalization method.

It can be shown [56] that a linear chain of intersecting spheres has the same depolarization coefficients as an infinite cylinder for $\xi = [4\sum_{k=1}^{\infty} k^{-3}]^{1/3} \approx 1.688$. It is important to note that two independent depolarization coefficients can simultaneously be "tuned" to correct values by adjusting only one free parameter ξ. As is well known, the depolarization coefficients in ellipsoids (an infinite cylinder being a particular case) determine the spectral positions of the resonances. Thus, the renormalization procedure gives the correct spectral locations of the optical resonances for a one-dimensional (1D) chain. The line shape of each resonance can still be described incorrectly. However, in the situation of a large fractal cluster, typical absorption and extinction spectra are superpositions of many collective resonances, and the line shapes of individual resonance are of little importance.

Another approach to estimating the parameter ξ is by analogy with the discrete dipole approximation (see [38–40]) in which bulk nonspherical particles are modeled by arrays of point dipoles located on a cubic lattice. In the first approximation, the polarizability of the dipoles is taken to be equal to that of an equivalent sphere with the radius R_m such that its volume is equal to the volume of the lattice cell, that is, $(4\pi/3)R_m^3 = l^3$. From this equality we find $\xi = l/R_m = (4\pi/3)^{1/3} \approx 1.612$.

Given a computer-generated renormalized ensemble of clusters, we can build the CDE (9.63) and solve it numerically to obtain all desirable optical constants. The CDE (9.63) can be written in the operator form [30,31], analogously to (9.24), except that the Hilbert space now has a finite dimensionality $3N$. We denote by $|d\rangle$ the $3N$-dimensional vector of dipole moments, and write

$$|d\rangle = \alpha(|E_{\text{inc}}\rangle + W_m|d\rangle) \tag{9.71}$$

The operator W_m in (9.71) is a square $3N \times 3N$ matrix rather than an integra operator W in (9.24), which is being emphasized here by using the subscript "m". I a basis of vectors $|i\alpha\rangle$, such that $d_{i\alpha} = \langle i\alpha|d\rangle$ (the Greek indexes denote the Cartesia components of the vectors), the matrix elements of W_m are $\langle i\alpha|W_m|j\beta\rangle =$ $k^3[A(kr_{ij})\delta_{\alpha\beta} + B(kr_{ij})r_{ij,\alpha}r_{ij,\beta}/r_{ij}^2]$.

The eigenvector expansion of the solution to (9.71) was proposed in [30,31] fo the quasistatic case ($R_g \ll \lambda$) and in [34] in the general case, and is similar to (9.30)

$$|d\rangle = \sum_n \frac{|n\rangle\langle n^*|E_{\text{inc}}\rangle}{\langle n^*|n\rangle[1/\alpha - w_n]} \tag{9.72}$$

where $|n\rangle$ are now the eigenvectors of W_m.

If we use (9.65) with $\sum_{i=1}^{N} \mathbf{d}_i \cdot \mathbf{E}^*_{\text{inc}}(\mathbf{r}_i) = \langle E_{\text{inc}}|d\rangle$, we can write for the extinction cross-section:

$$\sigma_e = \frac{4\pi k}{|\mathbf{E}_0|^2} \text{Im} \sum_n \frac{\langle E_{\text{inc}}|n\rangle\langle n^*|E_{\text{inc}}\rangle}{\langle n^*|n\rangle[1/\alpha - w_n]} \tag{9.73}$$

Now, we recall that $1/\alpha = 1/v\chi - i2k^3/3$ and $1/\chi = -(X + i\delta)$, where the spectral dependence of X and δ are illustrated in Fig. 9.4 (b), and write

$$\sigma_e = -\frac{4\pi k v}{|\mathbf{E}_0|^2} \text{Im} \sum_n \frac{\langle E_{\text{inc}}|n\rangle\langle n^*|E_{\text{inc}}\rangle}{\langle n^*|n\rangle[X + i(\delta + 2k^3 v/3) + vw_n]} \tag{9.74}$$

Equation (9.74) illustrates the importance of the parameters X and δ. The interaction of the monomers is weak and can be neglected when the "normalized" dimensionless eigenvalues vw_n are small compared to $X + i(\delta + 2k^3 v/3)$. By neglecting the eigenvalues in the denominator of (9.74), we immediately recover the first Born approximation. There are two distinct cases when such an approximation is valid. The first case is a nonresonant interaction, when $|X| \gg v\text{Re}\, w_n$. But even if $X + \text{Re}\, w_n$ can turn exactly to zero (resonant interaction), the absorption parameter δ can be still sufficiently large to make the first Born approximation accurate.

Further, we can introduce the "weighted" density of states $\Gamma(w', w'')$ according to

$$\Gamma(w', w'') = \sum_n \frac{\langle E_{\text{inc}}|n\rangle\langle n^*|E_{\text{inc}}\rangle}{\langle n^*|n\rangle} \delta(w' - \text{Re}\, w_n)\delta(w'' - \text{Im}\, w_n) \tag{9.75}$$

and rewrite (9.74) as

$$\sigma_e = -\frac{4\pi k v}{|\mathbf{E}_0|^2} \text{Im} \int \frac{\Gamma(w', w'')dw'dw''}{X + i(\delta + 2k^3 v/3) + v(w' + iw'')} \tag{9.76}$$

This formula is a convenient starting point for a family of analytical approximations. The familiar mean-field approximation can be obtained by assuming that the eigenvalues of W_m all lie in a small bound region in the complex plane, while the complex variable $X + i(\delta + 2k^3 v/3)$ is far from this region. Then, the density of states can be approximated as $\Gamma(w', w'') = N|\mathbf{E}_0|^2 \delta(w' - \text{Re}\, Q_1)\delta(w'' - \text{Im}\, Q_1)$, and the integration in (9.76) results in a formula similar to (9.45) without the self-energy term. The requirement for applicability of the mean-field approximation is, obviously, different than that for the first Born approximation. Namely, the eigenvalues do not need to be small, but rather quasidegenerate. Higher order approximations can be built by making the form of $\Gamma(w', w'')$ more complicated. As the first step, $\Gamma(w', w'')$ can be assumed to be constant in a certain bound rectangular area in the complex plane and zero outside, with the dispersion (first moments) determined from numerical diagonalization of a typical matrix W_m. This functional form still allows one to integrate (9.76) analytically. At higher levels of approximation, other moments of $\Gamma(w', w'')$ can be specified as well.

Note that for highly absorbing carbon material, the parameter δ can be much larger than the imaginary parts of the eigenvalues $v\,\text{Im}\, w_n$ (as well as the factor $2k^3 v/3$). In this case, it is sufficient to consider a 1D function $\Gamma(w')$. This is a good approximation in the quasistatic limit $\lambda \gg R_g$, when the imaginary parts of eigenvalues are proportional to the small factor $2k^3/3$ [34] and can be neglected. The complex eigenvalues of W_m are discussed in much more detail in Chapter 5, for the case of nonfractal, random and spherically symmetrical distribution of dipoles with the average interparticle distance $\sim \lambda$. The results of Chapter 5 are indicative of the fact that the imaginary parts of the eigenvalues in this case are still of the order of $2k^3/3$, and can be neglected for strongly absorbing soot. However, a calculation of the imaginary parts of the eigenvalues for a self-supporting fractal cluster, which is not small compared to λ, has not been performed to the best of our knowledge.

An important remark should be made regarding the influence of the renormalization procedure (9.68)–(9.70) on expressions of the form (9.74) and (9.76). The parameters X and δ do not depend on the geometry of the problem and, therefore, are not affected by the renormalization. However, the eigenvalues vw_n are changed as the result of renormalization. In particular, it is easy to see from (9.68)–(9.70) that the renormalized volume is $v' = v(\xi/2)^{3D/(3-D)}$. In general, the eigenvalues of the interaction matrix W_m do not scale with the parameter l, and it is impossible to write a similar relation between w_n and w'_n. However, this becomes possible in the quasistatic limit $\lambda \gg R_g$, when the intermediate- and far-zone terms in (9.10) and (9.11) can be neglected and the exponential factor $\exp(ix)$ can be set to unity. Then, from the form of the interaction matrix, it follows that $w'_n = w_n(l/l')^3 = w_n(2/\xi)^{9/(3-D)}$. By combining these two expressions, we obtain in the quasistatic limit: $v'w'_n = vw_n(2/\xi)^3$. We recall that ξ is the intersection parameter, and $1 < \xi \leq 2$. Thus, the intersection procedure effectively increases the normalized eigenvalues and, consequently, the interaction strength. The same tendency holds beyond the quasistatic limit, although the ratio $v'w'_n/vw_n$ becomes different for different n in this case.

Due to volume limitations, we have skipped the important question of orientational averaging in the dipole approximation. This averaging is trivial in the quasistatic case, and can be performed by averaging results for three orthogonal polarizations of the incident wave. However, the averaging becomes much more complicated in the case of finite k; see [57] for a further reference.

9.4.4. Numerical Examples

In this section, we illustrate the methods described above with a few numerical examples. We start with the perturbation expansion for the extinction cross-section

In Fig. 9.5, we plot the results of perturbative calculations of the extinction efficiency Q_e defined as

$$Q_e = \frac{\sigma_e}{k v_{\text{tot}}} \tag{9.7}$$

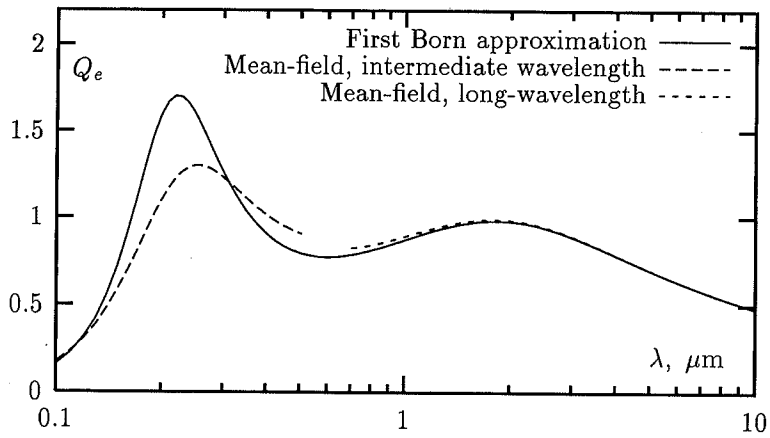

Figure 9.5. Perturbative calculations of the extinction efficiency Q_e for a cluster with $N = 2500$, $l = 2R_m = 0.02\,\mu$m, and $R_g \approx 33l = 0.66\,\mu$m.

The extinction efficiency is calculated for an ensemble of clusters with $N = 2500$, $l = 2R_m = 0.02\,\mu$m, and $R_g \approx 33l = 0.66\,\mu$m. In this figure, we compare the first Born approximation for Q_e obtained from (9.32) by retaining only the $k = 0$ term in the summation, compared to the first-order mean-field approximation (9.45) obtained by setting $\Sigma = 0$ in (9.45). We used the optical constants for carbon described in Section 9.3. The constant $Q_1 = B_1$ that is used in the mean-field approximation was calculated from the analytical formulas for the "intermediate" wavelength regime ($R_m \ll \lambda \ll R_g$) (9.60) and (9.61), and for the long-wavelength regime ($R_m \ll R_g \ll \lambda$) (9.62). The corresponding curves are plotted in the spectral regions where these regimes are valid. In the intermediate region $\lambda = R_g$, both analytical expressions for B_1 become inaccurate and numerical integration according to (9.58) should be performed. However, it is plausible to assume from the figure that the two curves will smoothly connect to each other near $\lambda = R_g$. Note that in the limit $kR_m \ll 1$, the first Born approximation also gives the "noninteracting" value of Q_e, that is, calculated for isolated spherical monomers.

While the mean-field approximation gives significantly different results from the first Born approximation for $\lambda \ll 1\mu$m, the difference becomes small for larger wavelengths. This might seem to be an indication of fast convergence of the perturbation series for large λ's. However, it is not the case. In fact, the coefficient B_1 becomes small in the long-wavelength limit [see Eq.(9.3)] due to the special symmetry of the dipole–dipole interaction. However, as we saw above, the dipole approximation is not accurate in the higher orders of the expansion, and the higher coefficients B_k can be large.

The deficiency of the mean-field approximation in the long-wavelength limit is most easily demonstrated with quasistatic calculations, in the limit $\lambda \gg R_g$. In Fig. 9.6, we compare the results of the first Born and the mean-field approximations [with the long-wavelength version of B_1 calculated according to (9.62)] to the numerical nonperturbative solution based on the expansion of all scattered fields into spherical

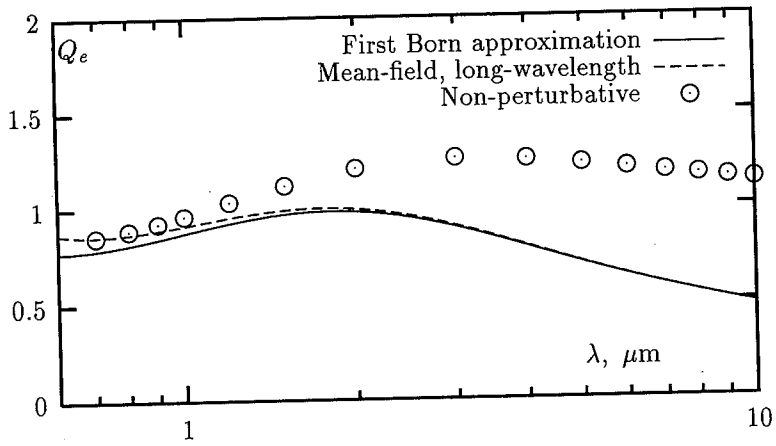

Figure 9.6. Perturbative and nonperturbative calculations of the extinction efficiency Q_e f cluster with $N = 100$, $l = 2R_m = 0.02\,\mu$m, and $R_g \approx 10.6l = 0.2\,\mu$m.

harmonics and considering boundary conditions at each spherical surface.[5] calculations are done for a small cluster with the following parameters: $N = 1$ $l = 2R_m = 0.02\,\mu$m, and $R_g \approx 10.6l = 0.2\,\mu$m, so that the condition $\lambda \gg R_g$ fulfilled everywhere in the spectral region shown in Fig. 9.6.

As can be seen from this figure, the perturbation expansion gives a dec agreement with the nonperturbative results for $\lambda \leq 1\,\mu$m. However, at $\lambda = 1\,\mu$m, non-perturbative solution is approximately two times larger. In general, nonperturbative solution decreases much more slowly with λ. Note that the spec dependence of the extinction cross section σ_e differs from that for the extinc efficiency Q_e by the factor $k \propto 1/\lambda$.

As the discrepancy between the perturbative and nonperturbative solut increases in the long-wavelength spectral range, the number of spherical harmo required for obtaining an accurate nonperturbative solution also grows. tendency is illustrated in Fig. 9.7, where we plot the extinction efficiency as a func of the maximum order of the spherical harmonics, L. We see that near $\lambda = 10$ accurate results are obtained for $L \sim 10$. This value grows for larger lambda, a optical properties of carbon become more metallic. However, even a calcul with only $N = 100$ and $L = 10$ requires ~ 600 Mb of memory in the quasistatic and twice as much for finite k's. Since the memory requirement grows as $\sim N$ calculations with significantly larger L's or N's seem to be problematic. Th especially true for clusters of metallic particles. Our estimates show that for s colloidal clusters in the visible and near-IR spectral ranges, the required L is o order of 100 (data not shown).

As an alternative method, we consider the dipole approximation coupled t geometrical renormalization of clusters described in Section 9.4.3. In Fig. 9.8 plot the results of calculations of Q_e in the dipole approximation for different v

[5]Fortran codes courtesy of D. Mackowski.

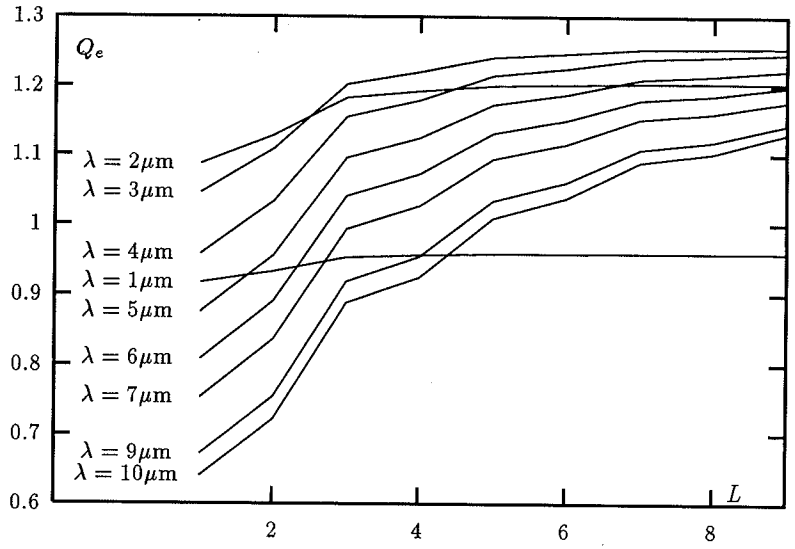

Figure 9.7. Extinction efficiency Q_e as a function of the maximum order L of the spherical harmonics involved in the nonperturbative calculation based on the expansion of all scattered fields into spherical harmonics and considering boundary conditions at each spherical surface (Fortran codes courtesy of D. Mackowski for more details see [49]). The calculations were performed in the quasistatic limit for a cluster with $N = 100$, $l = 2R_m = 0.02\,\mu$m and $R_g \approx 10.6l = 0.2\,\mu$m, and for different values of λ, from 1 to 10 μm.

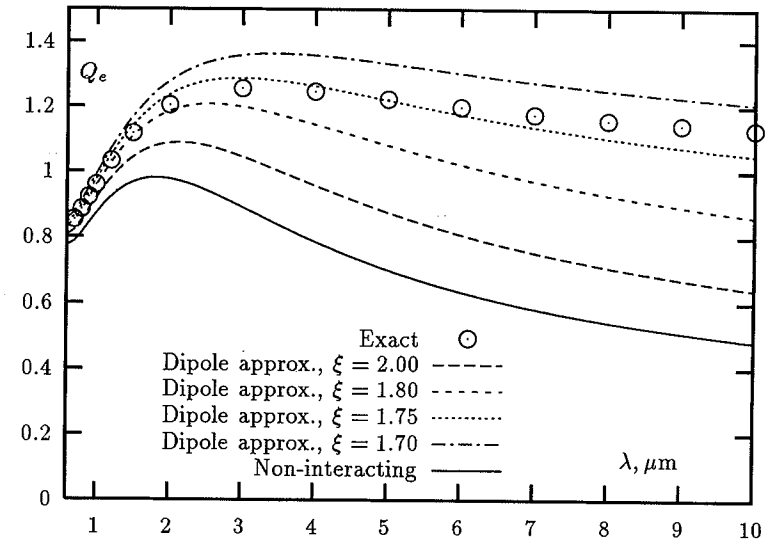

Figure 9.8. Extinction efficiency Q_e as a function of λ in the quasistatic limit. Solid curve — fist Born approximation (noninteracting limit). The $\xi = 2$ curve is the dipole approximation without geometrical renormalization of clusters. The centered symbols are the "exact" solution based on the multipole expansion.

of the intersection parameter ξ compared to the calculations based on the multipole expansion (referred to as "exact" in the figure caption) and to the first Born approximation. Since the latter can be obtained by considering isolated monomers, it is also referred to as the "non-interacting" approximation. The case $\xi = 2$ corresponds to the usual dipole approximation without renormalization.

Even without renormalization, the dipole approximation gives more accurate results than the first Born (noninteracting) approximation. But the introduction of geometrical intersections allows one to achieve much better accuracy. A good fit is obtained for $\xi = 1.75$. Note that, due to computational limitations, these results were obtained for single random realizations of computer-generated (renormalized) fractal clusters. However, the renormalization approach is statistical in nature, and we believe that ensemble averaging will increase the quality of the fit for a properly adjusted intersection parameter ξ. Nevertheless, the maximum deviation of the $\xi = 1.75$ curve from the "exact" result is only 2%.

Now, we turn our attention to the "weighted" density of states, $\Gamma(w', w'')$ defined by (9.75), and the analytical approximations that can be derived from simplification of the form of $\Gamma(w', w'')$. We restrict our consideration to the quasistatic limit, when the imaginary parts of all eigenvalues are small, and it is sufficient to consider a 1D function $\Gamma(w')$. The quasistatic analog of (9.76) is

$$\sigma_e = -\frac{4\pi k v}{|\mathbf{E}_0|^2}\,\mathrm{Im}\int \frac{\Gamma(w')dw'}{X + i\delta + vw'} \tag{9.78}$$

where we have also neglected the small term $2k^3v/3$. This can be rewritten for the efficiency Q_e as

$$Q_e = \frac{4\pi\delta}{N|\mathbf{E}_0|^2}\int \frac{\Gamma(w')dw'}{(X + vw')^2 + \delta^2} \tag{9.79}$$

A typical quasistatic density of states, calculated for an ensemble of clusters with $N = 1000$, is illustrated in Fig. 9.9. It is normalized by the condition $\int \Gamma(w')dw' = N|\mathbf{E}_0|^2$. The step-like function shown in Fig. 9.9 has the same normalization, first and second moments as the numerical $\Gamma(w')$.

By comparing Figs. 9.4 and 9.9, we can conclude that the complex variable $-1/\chi = X + i\delta$ always lies far in the complex plane from the region on the real axis occupied by the normalized eigenvalues vw_n [the region where $\Gamma(w')$ is not zero]. This, in turn, leads to the idea that the fine structure of $\Gamma(w')$ is not important. As we mentioned in Section 9.4.3, replacing $\Gamma(w')$ by a delta function with the same normalization and first moment results in the mean-field approximation. However, it can be seen from Fig. 9.9 that the first moment of $\Gamma(w')$ is equal to zero. This, indeed, follows from the expression (9.62) for $B_1 = Q_1$ in the limit $k \to 0$, and is a consequence of the spherical symmetry of the clusters and the tensor properties of the dipole–dipole interaction. Therefore, the mean-field approximation in the quasistatic limit is, essentially, equivalent to the first Born (noninteracting) approximation. This fact is also illustrated in Fig. 9.6.

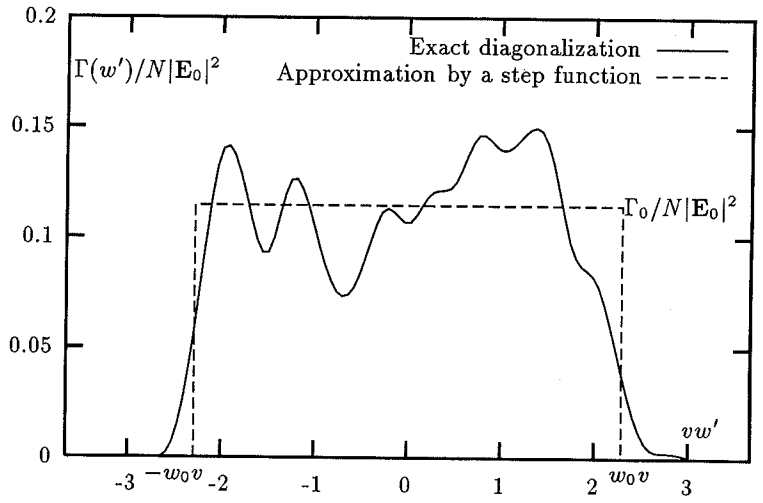

Figure 9.9. "Weighted" density of states $\Gamma(w')$ in the quasistatic limit, and its approximation by a step function with the equivalent normalization, first and second moments. The numerical diagonalization is performed for an ensemble of 10 clusters with $N = 1000$. The values of the constants are $vw_0 = 2.29$ and $\Gamma_0 = N|\mathbf{E}_0|^2/2w_0$.

To go beyond the mean-field approximation, we replace $\Gamma(w')$ by a step-like function, which preserves the second moment of $\Gamma(w')$ in addition to the first moment and normalization, as shown in Fig. 9.9 (see the figure caption for numerical values of the constants). By using the step-like function in (9.79), we obtain

$$Q_e = \frac{\pi\delta}{w_0}\int_{-w_0}^{w_0} \frac{dw'}{(X+vw')^2+\delta^2} \tag{9.80}$$

The integral can be easily evaluated, and results in

$$Q_e = \frac{2\pi}{vw_0}\left[\arctan\left(\frac{X+vw_0}{\delta}\right) - \arctan\left(\frac{X-vw_0}{\delta}\right)\right] \tag{9.81}$$

For clusters of touching spheres (without geometrical renormalization), vw_0 is a constant. From our calculations for computer-generated cluster–cluster aggregates, $vw_0 \approx 2.29$. Now, we recall that the renormalization results in $v'w_0' = (2/\xi)^3 vw_0$. Therefore, for a renormalized cluster, the extinction efficiency can be approximately written as

$$Q_e = \frac{2\pi}{2.29(2/\xi)^3}\left[\arctan\left(\frac{X+2.29(2/\xi)^3}{\delta}\right) - \arctan\left(\frac{X-2.29(2/\xi)^3}{\delta}\right)\right] \tag{9.82}$$

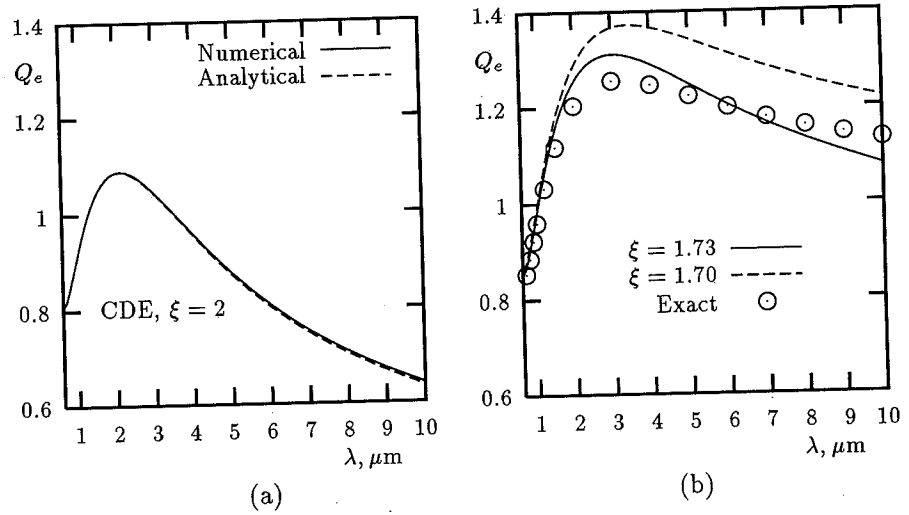

Figure 9.10. (a) Analytical expression (9.82) compared to numerical calculations in the dipole approximation without cluster renormalization ($\xi = 2$). (b) Analytical expression (9.82) for two different values of $\xi < 2$ compared to the exact result.

The results of calculations according to formula (9.82) are shown in Fig 9.10. First, in Fig 9.10 (a), we compare the analytical expression (9.82) with the results of numerical calculations in the dipole approximation without the geometrical renormalization ($\xi = 2$). The analytical and numerical data fit very accurately. In Fig 9.10(b), we plot Q_e given by (9.82) for two different values of $\xi < 2$ compared to the "exact" result (the one shown in Fig. 9.6 by circles). We see that the closest fit is achieved for $\xi \sim 1.73$. The curve with $\xi = 1.7$ gives a less accurate approximation of Q_e, but better reproduces the λ dependence in the long-wavelength region (up to a multiplicative constant). When comparing the results of the dipole approximation and the analytical formula (9.82) with the exact calculations which are shown in Fig. 9.10 (b) by circles, keep in mind that the latter were obtained by truncation of the maximum order of spherical harmonics, L. As seen in Fig. 9.7, the calculated value of Q_e still continues to grow for $L \sim 10$ and $\lambda > 2\,\mu$m. Our calculations were truncated at $L = 9$ due to computational limitations. But it can be stated with a reasonable amount of confidence that the "true" results for Q_e are somewhat larger than those shown, for example, in Fig. 9.10(b). This follows from the monotonic growth of Q_e as a function of L illustrated in Fig. 9.7. Therefore, the curve with $\xi = 1.7$ might be actually more accurate than the one with $\xi = 1.73$.

In conclusion of this section, we note that the value vw_0 [or the second moment of $\Gamma(w')$] can depend on the fractal dimension of the clusters. The fine features of $\Gamma(w')$ can also depend on less essential properties of the clusters, such as the type of lattice used in numerical calculations. For nonresonant carbon, these fine details of the density of states are largely insignificant. However, they become important in the

resonance situation, when the denominator in the formulas (9.76) and (9.78) can become purely imaginary and small. The resonance EM interaction in fractal clusters is considered theoretically in Chapter 8, and from the experimental point of view given in Chapter 7. Danilova discussed the phenomenological intersection parameter ξ for the case of resonance interaction and compared analytical and experimental results in [58].

9.5. FLUCTUATIONS OF LIGHT SCATTERED BY RANDOM SMOKE CLUSTERS

The well-known result (e.g., [14]) for the differential scattering cross-section of fractal clusters in the first Born approximation is

$$\frac{d\sigma_s}{d\Omega} \propto q^{-D} \qquad \text{if} \quad q \gg 1/R_g \tag{9.83}$$

where $\mathbf{q} = \mathbf{k} - \mathbf{k}'$ is the transmitted wavevector. This result is obtained by statistical averaging using the density–density correlation function (9.1), and is statistical in nature. The intensity of light scattered from a single random cluster can be different from (9.83). The statistical averaging implied in the derivation of (9.83) can be understood in two different ways. The first is ensemble averaging, over an ensemble of random realizations of clusters. One can also hope that if a single cluster is large enough, it's differential scattering cross-section approaches the ensemble average value, and the deviations decrease with the cluster size as $1/\sqrt{N}$ (self-averaging).

In this section, we show that the self-averaging can occur for random nonfractal clusters, but not for fractal aggregates with long-range correlations. In fact, we will show numerically that the relative dispersion of the scattered intensity in an ensemble of fractal cluster–cluster aggregates is always close to unity. A more detailed account is published in [23].

9.5.1. General Relations

The differential scattering cross-section can be calculated using the general definition (9.15) and the expression for the scattering amplitude $f(\mathbf{k}')$ either in the integral form (9.14) or the discretized version (9.64). In the first Born approximation, which will be used throughout this section, both formulas for $\mathbf{f}$ lead to the same result. For simplicity, we start from the discretized expression (9.64), and, by substituting $\mathbf{d}_i = \alpha \mathbf{E}_{\text{inc}}(\mathbf{r}_i) = \alpha \mathbf{E}_0 \exp(i\mathbf{k} \cdot \mathbf{r}_i)$, we obtain

$$\mathbf{f}(\mathbf{k}') = k^2 \alpha \left[\mathbf{E}_0 - \frac{(\mathbf{E}_0 \cdot \mathbf{k}')\mathbf{k}'}{k^2} \right] \sum_{i=1}^{N} \exp(i\mathbf{q} \cdot \mathbf{r}_i) \tag{9.84}$$

where $\mathbf{q} = \mathbf{k} - \mathbf{k}'$. The differential scattering cross-section can be easily obtained from the above expression

$$\frac{d\sigma_s}{d\Omega} = k^4 |\alpha|^2 |\mathbf{E}_0|^2 \sin^2[\psi(\mathbf{E}_0, \mathbf{k}')] \left| \sum_{i=1}^{N} \exp(i\mathbf{q} \cdot \mathbf{r}_i) \right|^2 \tag{9.85}$$

where $\psi(\mathbf{E}_0, \mathbf{k}')$ denotes the angle between $\mathbf{E}_0$ and $\mathbf{k}'$. The prefactor $k^4|\alpha|^2 \times |\mathbf{E}_0|^2 \sin^2[\psi(\mathbf{E}_0, \mathbf{k}')]$ does not depend on a random realization of the set $\{\mathbf{r}_i\}$ and, therefore, is the same for all clusters. In the case of scattering of a depolarized wave, we must replace $\sin^2[\psi(\mathbf{E}_0, \mathbf{k}')]$ by $\langle \sin^2\psi \rangle = 0.5$, and the above factor becomes simply a constant. In contrast, the factor $\left| \sum_{i=1}^{N} \exp(i\mathbf{q} \cdot \mathbf{r}_i) \right|^2$ in (9.85) is random and can vary from cluster to cluster.

When considering fluctuations of scattered light by different random clusters, we do not need to keep a factor that is common to all of them. Therefore, it is convenient to define the intensity of light scattered by some individual cluster as

$$I(\theta, \phi) = I(\mathbf{q}) = \left| \sum_{i=1}^{N} \exp(i\mathbf{q} \cdot \mathbf{r}_i) \right|^2 \tag{9.86}$$

where θ is the angle between the direction of the incident wavevector $\mathbf{k}$ and the direction of scattering, and ϕ is the azimuthal angle. The absolute value of $\mathbf{q}$ depends on the scattering angle θ as

$$q = k\sqrt{2(1 - \cos\theta)} \tag{9.87}$$

The intensity (9.86) coincides with the "real" intensity of the scattered light up to some constant in the case of a depolarized incident wave, and up to the ψ-dependent factor, $\sin^2[\psi(\mathbf{E}_0, \mathbf{k}')]$, for a polarized wave. The definition of scattered intensity (9.86) is suitable for the calculation of *relative* fluctuations, that is, for the dispersion of scattered intensity divided by the average scattered intensity. If we want to calculate *absolute* fluctuations, we need, of course, to keep all the prefactors. In this section, we will focus on relative fluctuations. The absolute value of fluctuations can always be reconstructed, provided the average scattered intensity is known.

Let us consider the intensity of light scattered by some number of fractal clusters randomly distributed in a certain volume. The distance between clusters is supposed to be large compared to the wavelength of the incident radiation, λ, and the distribution of clusters in space to be random and uncorrelated. Then, we can add the intensities of light scattered by each cluster, rather than the amplitudes.

The average scattered intensity $\langle I \rangle$ is defined as

$$\langle I \rangle = \langle I(\theta, \phi) \rangle = \lim_{M \to \infty} \frac{1}{M} \sum_{k=1}^{M} I_k(\theta, \phi) \tag{9.8}$$

where $I_k(\theta, \phi)$ is the intensity scattered by the kth cluster and M is the total number of clusters that scatter the light. With the use of (9.86), we can rewrite (9.88) as

$$\langle I \rangle = \lim_{M\to\infty} \frac{1}{M} \sum_{k=1}^{M} \sum_{i,j=1}^{N_k} \exp[i\mathbf{q} \cdot (\mathbf{r}_i^{(k)} - \mathbf{r}_j^{(k)})] \tag{9.89}$$

where N_k is the number of monomers in the kth cluster, and $\mathbf{r}_i^{(k)}$ is the coordinate of the ith monomer in kth cluster.

For an ensemble of spherically symmetrical (on average) clusters, the dependence of $\langle I \rangle$ on ϕ is weak (it vanishes for an infinite ensemble); therefore, we will use the notation $\langle I \rangle = \langle I(\theta) \rangle = \langle I(q) \rangle$, where q is defined by (9.87).

If we detect the scattered light from just one cluster, it can be much different from $\langle I \rangle$. A convenient measure of these variations is the standard deviation (dispersion), σ_I:

$$\sigma_I^2 = \langle I^2 \rangle - \langle I \rangle^2 \tag{9.90}$$

The value of σ_I characterizes possible deviations of I_k from $\langle I \rangle$ calculated for an infinite ensemble of clusters and has a simple mathematical meaning: The probability that an individual I_k lies within the interval $\langle I \rangle \pm \sigma_I$ is approximately two-thirds.

In the case of a finite M, one can be interested in a measure of fluctuations of the average value (9.88) itself [the "lim" sign in this case should, of course, be omitted in (9.88) and (9.89)]. If we register the scattered light from different ensembles of clusters consisting of some finite number of clusters M, we will come up with different results. We can define the standard deviation $\sigma_I^{(M)}$ of these random values in the usual way. The relation between $\sigma_I^{(M)}$ and $\sigma_I \equiv \sigma_I^{(1)}$ is well-known from mathematical statistics:

$$\sigma_I^{(M)} = \frac{\sigma_I}{\sqrt{M}} \tag{9.91}$$

The actual value of M depends on the scheme of the experiment. In one possible setting, the scattering volume is small enough (e.g., due to focusing a laser beam) and contains only one cluster at a time. Because of the random motion of clusters, it contains different clusters in different moments of time. In this case, one can register scattered radiation for some large period of time (excluding the periods when the volume contains no clusters at all and the signal is zero) and calculate the time-averaged intensity and its standard deviation, which coincides with σ_I. If the volume contains an average of M clusters at a given time, the measured standard deviation would be $\sigma_I^{(M)}$. As will be shown numerically in Section 9.5.2, σ_I is universal for cluster–cluster aggregates over a wide range of scattering angles. The relation (9.91) can be used to find the average number of clusters in the scattering volume (and, hence, the number density of clusters).

9.5.2. Monodisperse Clusters

First, we consider monodisperse ensembles of clusters consisting of N monomers each. The task of calculating σ_I includes finding two average values: $\langle I \rangle$ and $\langle I^2 \rangle$. Apart from calculating the dispersion (Eq. 9.90), $\langle I \rangle$ is interesting by itself and is experimentally measurable. It is well known that the pair correlation function $p(r)$ (9.1) can be used to calculate $\langle I \rangle$. Indeed, for a monodisperse ensemble, (9.89) can be simplified to

$$\langle I \rangle = N + N(N-1)\langle \exp(i\mathbf{q} \cdot \mathbf{r}_{ij}) \rangle \tag{9.92}$$

where $\mathbf{r}_{ij} = \mathbf{r}_i - \mathbf{r}_j$, and only distinct monomers belonging to the same cluster are considered. Now, we can use the function $p(r)$ to calculate $\langle \exp(i\mathbf{q} \cdot \mathbf{r}_{ij}) \rangle$:

$$\langle \exp(i\mathbf{q} \cdot \mathbf{r}_{ij}) \rangle = \int_0^\infty p(r) \exp(i\mathbf{q} \cdot \mathbf{r}_{ij}) \frac{dr \sin\theta \, d\theta \, d\phi}{4\pi} \tag{9.93}$$

After performing the angular integration, (9.93) simplifies to

$$\langle \exp(i\mathbf{q} \cdot \mathbf{r}_{ij}) \rangle = \int_0^\infty p(r) \frac{\sin qr}{qr} dr \tag{9.94}$$

In the case of $D < 2$ and $q \gg R_g^{-1}$, we can calculate the integral (9.94) without specifying the form of the cutoff function for $p(r)$, similarly to the calculation of the coefficient B_1 in Section 9.4.2. Indeed, in this case the cutoff function can be set to unity, and the result is

$$\langle \exp(i\mathbf{q} \cdot \mathbf{r}_{ij}) \rangle = \frac{a\Gamma(D-1)\sin[\pi(D-1)/2]}{N(ql)^D} \tag{9.95}$$

In the other limiting case, $q \ll R_g^{-1}$, sin (qr) in (9.94) can be expanded in a power series, and the result of integration up to the lowest nonzero power of q is

$$\langle \exp(i\mathbf{q} \cdot \mathbf{r}_{ij}) \rangle = 1 - (qR_g)^2/3 \tag{9.96}$$

As follows from (9.96) and (9.92), $\langle I(\theta = 0) \rangle = N^2$, which means that the forward scattering is always coherent in the first Born approximation.

From (9.95) and (9.92), it can be concluded that the minimum possible value of $\langle I \rangle$ is N, which can be reached for large values of q. For the backscattering, when the value of q is maximum, the expression for $\langle I \rangle$ becomes $\langle I \rangle \approx N[1 + 5 \times 10^{-2}(\lambda/l)^D]$, where we used the numerical values for all the coefficients (assuming $D = 1.8$). The characteristic value of λ is $\lambda_c \approx 5.4l$, so that $\langle I \rangle$ approaches its lower bound for $\lambda \ll \lambda_c$. However, the above inequality contradicts the fundamental assumption of this chapter that λ is much larger than monomer size R_m (or lattice unit, l). Therefore, in the spectral region where the monomers are optically small, $kR_m \ll 1$, the first term in (9.92) can be neglected.

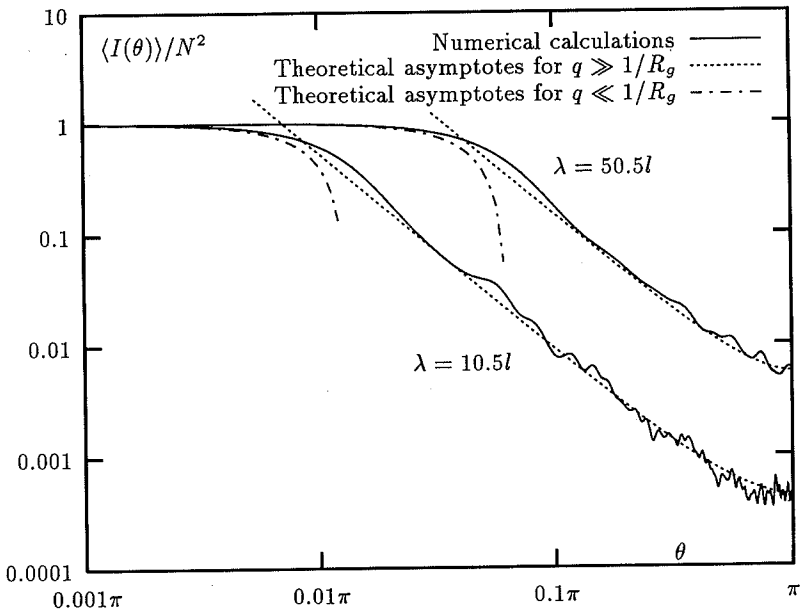

Figure 9.11. Average intensity of the scattered light as a function of the scattering angle θ for $\lambda = 10.5l$ and $\lambda = 50.5l$. Calculations were performed for a computer-generated monodisperse ensemble of 40 random cluster–cluster aggregates consisting of $N = 10{,}000$ monomers each, similar to the one shown in Fig. 9.1. Noninteger values of λ/l are chosen to avoid lattice effects. The definition of I is given in Eq. (9.86).

The theoretical asymptotes (9.95) and (9.96), along with the results of numerical calculations for $\langle I\rangle$ for different values of λ, are illustrated in Fig. 9.11 (see the figure caption for details).

Whereas $\langle I\rangle$ is defined by $p(r)$, one needs a higher order correlation function for the calculation of $\langle I^2\rangle$. Indeed, the definition of $\langle I^2\rangle$, analogous to (9.89), contains a fourfold summation, which, after grouping together the terms with different indexes matching each other, turns to

$$\langle I^2\rangle = N(2N-1) + 4N(N-1)^2\langle\exp(i\mathbf{q}\cdot\mathbf{r}_{ij})\rangle + N(N-1)(N^2-3N+3)\langle\exp(i\mathbf{q}\cdot\mathbf{r}_{ijkl})\rangle \tag{9.97}$$

where $\mathbf{r}_{ijkl} = \mathbf{r}_{ij} - \mathbf{r}_{kl}, i \neq j, k \neq l$ and any of the pair of indexes (i,j) can coincide with any of the pair (k,l). It is easy to show that $\langle\exp(i\mathbf{q}\cdot\mathbf{r}_{ijkl})\rangle$ is expressed through the four-point correlation function, $p_4(r)$, which was introduced in Section 9.2 (see also Fig. 9.3), exactly in the same form as in Eq. (9.94) with $\mathbf{r}_{ij}$ being replaced by $\mathbf{r}_{ijkl}$ and p by p_4.

We now turn to the numerical results for fluctuations that are presented in Fig. 9.12. In this calculation, we allowed θ to change from 0 to 2π, so that the "observer"

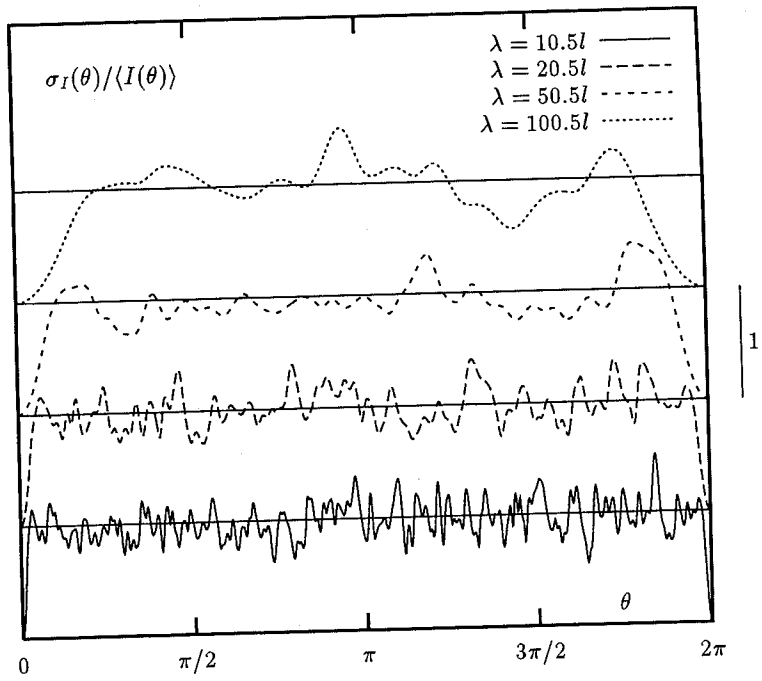

Figure 9.12. Relative fluctuations $\sigma_I(\theta)/\langle I(\theta)\rangle$ for different wavelengths as functions of the scattering angle θ. For each curve, the horizontal line corresponds to the level $\sigma_I/\langle I\rangle = 1$; the distance between the nearest horizontal lines is 1; and $\sigma_I(0)/\langle I(0)\rangle = \sigma_I(2\pi)/\langle I(2\pi)\rangle = 0$. Calculations are performed for the same ensemble of computer-generated clusters as in Fig. 9.11. Note that θ is allowed to change from 0 to 2π (unlike the usual spherical system of coordinates where $0 \leq \theta \leq \pi$), so that the "observer" makes a complete revolution from the "forward' direction of scattering to the "backward" direction and back to "forward".

makes a whole revolution from the "forward" direction of scattering to the "backward" direction and back to "forward". In the usual spherical system of coordinates, this corresponds to θ varying from 0 to π, then changing φ to $\phi + \pi$, and θ varying θ back from π to 0. Note that, for a finite ensemble of random clusters, the result is not necessarily symmetrical with respect to the point $\theta = \pi$. However, it must be symmetrical for an infinite ensemble of spherically symmetrical (or average) clusters; this follows from the fact that neither σ_I nor $\langle I\rangle$ can depend on φ in this case.

First, we consider the domains of θ where the asymptote (9.95) is valid. The characteristic values of θ_c [defined from the condition $q(\theta_c) = R_g^{-1}$] are 5.4×10^{-3} for $\lambda = 10.5l$, $1.0 \cdot 10^{-2}\pi$ for $\lambda = 20.5l$, $2.6 \times 10^{-2}\pi$ for $\lambda = 50.5l$, and 0.16π for $\lambda = 100.5l$. One can easily see that the value of $\sigma_I/\langle I\rangle$ fluctuates near unity in $\theta_c \ll \theta \ll 2\pi - \theta_c$.[6] It should be noted that for a finite ensemble, $\sigma_I/\langle I\rangle$ is a random quantity itself. Since there is no noticeable systematic dependence on θ in the domain

[6] As can be seen from Figs. 9.11 and 9.12, there is no need for *strong* inequalities here.

defined above, we can perform additional averaging of $\sigma_I/\langle I\rangle$ over θ, the results for this averaging are (up to the third significant figure): 0.98 for $\lambda = 10.5l$, 1.00 for $\lambda = 20.5l$, 0.96 for $\lambda = 50.5l$, and 1.01 for $\lambda = 100.5l$.

The numerical data suggest that the value of the relative fluctuations of the intensity of light scattered by cluster–cluster aggregates is very close to unity and statistically independent of the scattering angle θ, as long as θ lies in the domain defined above. This is true for a wide range of wavelengths λ. However, for very large λ, the domain of θ shrinks and becomes essentially empty when $\lambda = 4\pi R_g$.

9.5.3. Polydisperse Clusters

Now, we consider a polydisperse ensemble of clusters, that is, an ensemble containing clusters with different N's. We first look at the case of large q, when the condition $q \gg R_g^{-1}$ is fulfilled for almost every cluster in the ensemble.

We can calculate $\langle I\rangle$ by performing an additional averaging over N in Eq. (9.92). In the case of large q, this averaging leads to

$$\langle I\rangle = \langle N\rangle\{1 + a\Gamma(D-1)\sin[\pi(D-1)/2]/(ql)^D\} \tag{9.98}$$

It is natural to assume that the intensity scattered by some individual cluster I_k can be represented as

$$I_k = N_k J_k \tag{9.99}$$

where N_k and J_k are statistically independent random variables, and

$$\langle J\rangle = 1 + a\Gamma(D-1)\sin[\pi(D-1)/2]/(ql)^D \tag{9.100}$$

Then, ensemble averaging of (9.99) results in (9.98).

For a monodisperse ensemble, J_k coincide with I_k up to some constant, common for each cluster. Therefore, the relative dispersion of J, $\sigma_J/\langle J\rangle$, coincides with the relative dispersion of I in a monodisperse ensemble.

Further, we can use (9.99) to calculate the relative dispersion of scattered intensity in a polydisperse ensemble in terms of that in a monodisperse ensemble and the dispersion of the random variable N. Straightforward algebra yields

$$\frac{\sigma_I}{\langle I\rangle} = \frac{\sigma_J}{\langle J\rangle}\sqrt{\frac{\sigma_N^2}{\langle N\rangle^2}\left(1 + \frac{\langle J\rangle^2}{\sigma_J^2}\right) + 1} \tag{9.101}$$

From the numerical results of Section 9.5.2, we know that $\sigma_J/\langle J\rangle$ is very close to unity. By substituting this value into (9.101), we obtain

$$\frac{\sigma_I}{\langle I\rangle} = \sqrt{2\frac{\sigma_N^2}{\langle N\rangle^2} + 1} \tag{9.102}$$

It follows from formula (9.102) that $\sigma_I/\langle I\rangle$ is always close to unity, even for very polydisperse ensembles. The value of $\sigma_N/\langle N\rangle$ cannot be much > 1 for any physically reasonable distribution of N. For example, if N is uniformly distributed from 0 to $N_{\max}$, this value is equal to $1/\sqrt{3}$. If the distribution has two sharp peaks of equal height near N_1 and N_2, it is equal to $|N_1 - N_2|/(N_1 + N_2)$.

In order to verify Eq. (9.101), we calculated $\sigma_I/\langle I\rangle$ for a polydisperse ensemble of 100 clusters. The number of particles in a particular cluster was found from the Gaussian probability distribution with the average $\langle N\rangle = 5000$ and the dispersion[7] $\sigma_N = \sqrt{\langle N^2\rangle - \langle N\rangle^2} = 2000$. The ratio $\sigma_N/\langle N\rangle$ for this ensemble is $\simeq 0.37$. The calculations were done for two different values of λ. After additional averaging over angles (as described in Section 9.5.2), the results obtained are as follows: $\sigma_I/\langle I\rangle = 1.109$ for $\lambda = 10.5$, and $\sigma_I/\langle I\rangle = 1.087$ for $\lambda = 20.5$. The results following from the theoretical formula (9.101) and the corresponding results for a monodisperse ensemble ($\sigma_J/\langle J\rangle$) are 1.109 and 1.120, respectively. As we see, the results match closely. For the case of $\lambda = 10.5$, the difference is only in the fifth figure.

9.5.4. Fluctuations of Light Scattered by Trivial (Nonfractal) Clusters

It is interesting to compare the fluctuations of light scattered by fractal and by trivia ($D = 3$) clusters. In this Section, we discuss fluctuations in light intensity scattere from such systems, restricting consideration to only monodisperse ensembles.

To model random nonfractal clusters, we use the algorithm of randomly close packed hard spheres. In this algorithm, one first chooses a volume to be occupied b a cluster. In our simulations it is a sphere of radius R_s ("s" standing for "sphere" since we intended to build clusters that are spherically symmetrical. Then, monome are randomly placed inside the volume. At each step, the intersection condition checked: If the newly placed monomer approaches any of the previously placed on closer than the distance l, this step is rejected and the next random position is trie In this way, each monomer can be thought of as a hard sphere of radius $l/2$. T procedure stops when a large number of tries is consequently rejected. In o simulations, this number was chosen to be 2×10^7. This algorithm allows one achieve a fairly dense packaging. Consequently, we have packed 40 differe clusters with an average of 9200 monomers per cluster into a spherical volume wi radius $R_s = 14.2l$. The volume fraction occupied by the particles was ≈ 0.40. F comparison, it is ≈ 0.52 in the case of a simple cubic lattice and can be even low for some other types of lattices. The minimum distance from a given monomer to nearest neighbor was very close to l; the maximum distance varied from $1.2l$ to 1. Although this ensemble of clusters was not completely monodisperse, the variati of N was very small: The ratio of the standard deviation of N and the mean was equ to 2.4×10^{-3}.

[7] These parameters characterize the porbability distribution according to which the values of N w picked for each cluster. The actual parameters of the ensemble were slightly different: $\langle N\rangle = 53$ $\sigma_N = 1953$.

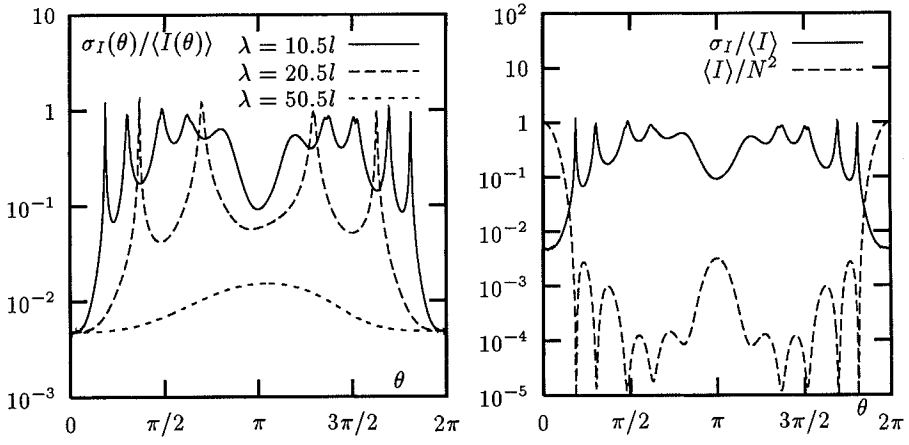

(a) (b)

Figure 9.13. (a) Relative fluctuations $\sigma_I(\theta)/\langle I(\theta)\rangle$ for random close-packed nonfractal clusters ($D = 3$) packed in a sphere of the radius $R_s = 14.2l$, for different wavelengths. (b) Relative fluctuations, $\sigma_I(\theta)/\langle I(\theta)\rangle$, compared to the average scattered intensity $\langle I\rangle$ for the same ensemble of clusters and $\lambda = 10.5l$.

The results of numerical simulations of $\sigma_I/\langle I\rangle$ for the ensemble of 40 clusters described above are shown in Fig. 9.13(a). As in Section 9.5.3, the scattering angle θ varies from 0 to 2π. First, we notice the strong and systematic dependence of $\sigma_I/\langle I\rangle$ on θ. [For fractal clusters, this dependence looks like statistical noise (cf Fig. 9.12)]. Second, for most angles the value of $\sigma_I/\langle I\rangle$ is significantly < 1 and decreases when λ grows. This dependence on λ is anticipated, because if there are many monomers in the volume λ^3, a cluster becomes optically similar to a dielectric sphere, and its random structure is of no importance. But this is not the case for fractal clusters; they are geometrically different and random on all scales up to the maximum scale R_g. As seen from Fig. 9.12, $\sigma_I/\langle I\rangle$ for fractal clusters is on the order of 1, even for $\lambda = 100.5l$. But for nonfractal clusters, $\sigma_I/\langle I\rangle$ is much smaller, on the order of 10^{-2} for $\lambda = 50.5l$.

The second feature of Fig. 9.13(a) is the presence of sharp maxima in $\sigma_I/\langle I\rangle$, where it becomes on the order of 1. These maxima occur for the angles θ at which $\langle I(\theta)\rangle$ has a minima [see Fig. 9.13(b)].

The problem of fluctuations can be solved exactly for spherically symmetrical random clusters, provided the positions of monomers in clusters are absolutely uncorrelated. This is not the case for the close-packed clusters discussed above, because in this model monomers cannot approach each other closer than l, which brings about short-range correlations. It is clear that the model of totally uncorrelated clusters (random gas) is not exact since the monomers act like hard spheres during aggregation. However, theoretical results for uncorrelated clusters help explain the main features shown in Fig. 9.13.

Consider a "random gas" of uncorrelated particles inside a spherical volume of radius R_s. The ensemble-average quantities $\langle\exp(i\mathbf{q}\cdot\mathbf{r}_i)\rangle$, $\langle\exp(i\mathbf{q}\cdot\mathbf{r}_{ij})\rangle$, and $\langle\exp(i\mathbf{q}\cdot\mathbf{r}_{ijkl})\rangle$ can be obtained from straightforward integration and are as follows:

$$\langle\exp(i\mathbf{q}\cdot\mathbf{r}_i)\rangle = \varphi(qR_s) \equiv \frac{3}{(qR_s)^3}[\sin(qR_s) - qR_s\cos(qR_s)] \tag{9.103}$$

$$\langle\exp(i\mathbf{q}\cdot\mathbf{r}_{ij})\rangle = \varphi^2(qR_s) \tag{9.104}$$

$$\langle\exp(i\mathbf{q}\cdot\mathbf{r}_{ijkl})\rangle = \varphi^4(qR_s) \tag{9.105}$$

The values of $\langle I\rangle$ and $\langle I^2\rangle$ can be found according to (9.92) and (9.97), with the use of (9.103)–(9.105). The expression for $\langle I\rangle$ is

$$\langle I\rangle = N + N(N-1)\varphi^2(qR_s) \tag{9.106}$$

and the expression for $\sigma_I/\langle I\rangle$ is (in the limit of large N)

$$\frac{\sigma_I}{\langle I\rangle} = \frac{\sqrt{1 - 4\varphi^2 + 3\varphi^4 + 2\varphi^2(1-\varphi^2)N}}{1 + \varphi^2 N} \tag{9.107}$$

If $\varphi(qR_s)$ turns to zero for some value of q, this means that $\sigma_I/\langle I\rangle$ has a maximum and is on the order of 1 for this q. At the same time, the average scattered intensity (9.106) has a minimum.

The function $\varphi(x)$ becomes exactly zero if x is a solution to $\tan(x) = x$. The first root of this equation is $x \approx 1.43\pi$. The corresponding scattering angle is defined by $\cos\theta = 1 - 0.26(\lambda/R_s)^2$. This equation has a solution only if $\lambda < 2.8R_s$. In Fig. 9.13, we have sharp maxima in $\sigma_I/\langle I\rangle$ for $\lambda = 10.5l$ and $\lambda = 20.5l$, but there are no sharp maxima for $\lambda = 50.5l$. For the clusters considered, $R_s = 14.2l$, and the critical value of λ is $39.7l$. We see that $\lambda = 50l$ exceeds the critical value and, therefore, the corresponding curve in Fig. 9.13 has no sharp maxima.

Now, we analyze the expression (9.107) in more detail. First, when $N \to \infty$, this expression assumes the form

$$\frac{\sigma_I}{\langle I\rangle} = \sqrt{\frac{2(1/\varphi^2 - 1)}{N}} \tag{9.108}$$

As one would expect, the relative fluctuations are proportional to $1/\sqrt{N}$. To obtain (9.108), we took the limit $N\varphi^2 \gg 1$. This condition can be expressed in terms of the density ν of monomers in clusters, where $N = 4\pi R_s^3\nu/3$. By using (9.103), we find that, in order to obtain (9.108), the following inequalities must hold

$$\nu \gg \frac{1}{12\pi}q^3 \quad \text{if} \quad qR_s \sim 1 \tag{9.109}$$

$$\nu \gg \frac{qR_s}{12\pi}q^3 \quad \text{if} \quad qR_s \gg 1 \tag{9.110}$$

The condition is always fulfilled if $qR_s \ll 1$, since $\varphi(0) = 1$. Note that in order to derive (9.109) and (9.110), we assumed that $\tan(qR_s) \neq qR_s$ and $\sin(qR_s)$, $\cos(qR_s) \sim 1$. As discussed above, if $\tan(qR_s) = qR_s$, $\varphi(qR_s)$ turns exactly to zero, the condition $N\varphi^2 \gg 1$ cannot be fulfilled.

The above inequalities show that in order to observe the $1/\sqrt{N}$ dependence for the fluctuations, one needs to have many monomers in the volume q^{-3}. This condition depends on the value of qR_s and is stronger when $qR_s \gg 1$. We emphasize that for fractal clusters we can never obtain the $1/\sqrt{N}$ dependence for relative fluctuations (see, e.g., the curve in Fig. 9.12 for $\lambda = 100.5l$). The reason is that the fractal clusters are disordered on all scales up to the maximum scale R_g, whereas trivial random clusters become homogeneous on scales larger than $1/\sqrt[3]{v}$.

Now, we turn our attention to the nature of the sharp maxima in $\sigma_I/\langle I \rangle$, which are seen in Fig. 9.13(a). As mentioned above, these maxima coincide with the diffraction minima of the average scattered intensity. The diffraction minima occur because within the first Born approximation, and for certain scattering angles, the EM fields produced by monomers in a cluster almost exactly cancel each other due to destructive interference. As a result, the scattered field for these scattering angles is produced, in fact, by a very few monomers, rather than by the whole cluster. This results in strong relative fluctuations.

9.6. ABSORPTION OF LIGHT BY SMOKE CLUSTERS PLACED IN A WATER DROPLET

Soot clusters often form agglomerates with water microdroplets, especially in the clouds [59–63]. Naturally, this might be expected to lead to dramatic changes in the optical characteristics. In this section, we obtain qualitative results concerning the *absorption* cross-section of such composite microdroplets in the first Born approximation, with an account of the fractal morphology of carbon soot clusters. Our consideration includes the nonfractal homogeneous distribution of carbon inclusions as a limiting case. A more detailed account can be found in [64].

The theoretical treatment in this section is somewhat different from the rest of the chapter. The small parameter of the perturbation expansion will not be χ, as above, but the volume fraction of carbon soot inside a water droplet. The microdroplet radius will be denoted by R_d ("d" standing for "droplet"), and its volume by $v_d = (4\pi/3)R_d^3$, so that the small parameter of the expansion is v_{tot}/v_d, with v_{tot} still being the total volume of carbon inclusions. It is not assumed, however, that the carbon inclusions in a microdroplet form one self-supporting cluster, or are built from spherical monomers. The only important quantity entering the calculations will be the average density of inclusions, $\langle \rho(\mathbf{r}) \rangle$, where the averaging is performed over an ensemble of droplets of the same radius with random carbon inclusions inside. Correspondingly, the results obtained in Section 9.6.1 are of a statistical nature.

9.6.1. Introductory Remarks and Review

When soot particles are placed inside a water droplet, they are no longer exited by a plane wave, but rather by internal modes of a high-quality optical resonator. To complicate things further, the resonator modes can effectively couple to the modes of clusters themselves.

There have been a considerable number of experimental [65–70] and theoretical [51,71–78] studies of scattering and absorbing properties of inhomogeneous spheres. The simplest model for a water droplet with an inclusion inside is a spherical dielectric particle with an eccentric spherical inclusion. An exact formal solution to the problem of light scattering and absorption by such composite spheres was obtained by Borghese et al. [72] and generalized for the case of multiple arbitrarily positioned spherical inclusions by Borghese et al. [75] and Fuller [51,52,76,79]. The solutions were obtained by the vector spherical harmonic (VSH) expansion of electrical fields inside the homogeneous spherical regions and satisfying the boundary conditions at all the discontinuity surfaces. Even in the case of one spherical inclusion, the solution must be obtained from an infinite-order system of linear equations. As discussed in Section 9.4.3, the VSH expansion is truncated at some maximum order L, and the system contains $\sim L^2$ equations [72]. When multiple inclusions are considered, the number of equations is further increased, which makes the problem very complicated numerically. Also, the approach based on the consideration of the exact boundary conditions requires a knowledge of the exact geometry of the problem before the time-extensive calculations. This fact complicates the averaging of solutions over a random distribution of inclusions inside water droplets.

An alternative approach based on perturbation theory was developed by Kerker et al. [71] and Hill et al. [77]. According to their method, the dielectric function of an inhomogeneous sphere is represented as a sum of a constant (unperturbed) value and a small coordinate-dependent perturbation. In the zeroth-order approximation, the field inside the droplet is calculated within the assumption that the perturbation of the dielectric function is equal to zero. This field is given by the Mie expansion in terms of the VSH. In the next iteration, the field in the zeroth-order approximation induces some additional polarization (or, equivalently, current) in the volume proportional to the perturbation of the dielectric function. This additional polarization can be used to calculate changes of scattering and absorbing characteristics of the inhomogeneous sphere as compared to the homogeneous (unperturbed) one. A big advantage of this method is that it allows one to perform averaging over random perturbations. However, it has a drawback. As was pointed out by Hill et al. [77], the internal field must be computed iteratively. That is, the additional polarization calculated in the first iteration described above should produce some additional internal electrical field, which, in turn, gives rise to additional polarization (now proportional to the unperturbed dielectric function), and so on. Physically this means that the modes of a spherical resonator are coupled to the modes of the perturbation of the dielectric function. In order for a finite-order approximation to be accurate, it is necessary that the perturbation expansion of any physical

quantity under consideration converges. In Section 9.6.2, we show that, in general, this is not the case. More specifically, this expansion always diverges for physical quantities related to scattering (such as the differential scattering cross-section). However, the perturbation expansion converges for the absorption cross-section when the imaginary part of the unperturbed dielectric function is zero (or sufficiently small).

We will use the above fact to calculate absorption cross-sections of carbon smoke particles inside spherical water droplets in the first order of the perturbation theory. The perturbation expansion is mathematically similar to that of Kerker et al. [71] and Hill et al. [77]. The water itself is assumed to be nonabsorbing. We perform calculations for a fractal distribution of carbon inclusions with a power-law dependence of the density on the distance from the center of a water droplet; the case of trivial (nonfractal) geometry is considered as a limiting case when $D = 3$.

The approach developed below applies to any spherical highly transparent microcavities doped with strongly absorbing inclusions with the fractal dimension from 1 to 3, not just to carbon soot inside water droplets. However, the numerical results are strongly dependent on the refractive index of the host. The difference between microdroplets with the refractive index of water (~ 1.33) and of sulfate (~ 1.52) was demonstrated by Fuller [52,79].

9.6.2. Formulation of the Model

Consider a plane monochromatic wave of the form (9.7) incident on a spherical water droplet of a radius R_d containing a carbon soot cluster inside. The physical system under consideration can be characterized by a dielectric function of the form

$$\varepsilon(\mathbf{r}) = \begin{cases} \varepsilon_1 + (\varepsilon_2 - \varepsilon_1)\rho(\mathbf{r}) & r \le R_d \\ 1, & r > R_d \end{cases} \tag{9.111}$$

Here ε_1 and ε_2 are the dielectric constants of water and carbon, respectively, and $\rho(\mathbf{r})$ is the density of carbon inclusions inside the droplet, normalized by the condition

$$\int_{V_d} \rho(\mathbf{r}) d^3\mathbf{r} = v_{\text{tot}} \tag{9.112}$$

where v_{tot} is the total volume occupied by carbon and $\int_{V_d}$ denotes integration over the spatial area defined by $r \le R_d$ ($\int_{V_d} d^3\mathbf{r} = v_d$). We assume that the volume fraction of carbon is small, so that the small parameter of the problem is v_{tot}/v_d. We also assume that $\rho(\mathbf{r}) = 0$ for $r > R_d$, that is, the soot cluster is completely covered by water.

In our notations, $\rho(\mathbf{r})$ denotes the exact density of carbon inclusions for some given random realization of a soot cluster. As such, $\rho(\mathbf{r}) = 1$ if the radius vector $\mathbf{r}$ lies in the area occupied by carbon, and $\rho(\mathbf{r}) = 0$ otherwise. We will see that for a calculation of some average physical characteristics, such as absorption, one needs

to average $\rho(\mathbf{r})$ over random realizations of carbon soot clusters. We denote the average density by $\langle\rho(\mathbf{r})\rangle$; it can be interpreted as the probability to find some given point $\mathbf{r}$ inside a droplet occupied by carbon. If $\langle\rho(\mathbf{r})\rangle$ is bound everywhere inside the sphere, the condition $v_{\text{tot}}/v_d \ll 1$ implies that $\langle\rho(\mathbf{r})\rangle \ll 1 \forall \mathbf{r}$.

The integral equation for the electric field $\mathbf{E}(\mathbf{r})$ analogous to (9.5) has the form

$$\mathbf{E}(\mathbf{r}) = \mathbf{E}_{\text{inc}}(\mathbf{r}) + \int_{V_d} \boldsymbol{G}(\mathbf{r} - \mathbf{r}') \frac{\varepsilon(\mathbf{r}') - 1}{4\pi} \mathbf{E}(\mathbf{r}') d^3\mathbf{r}' \tag{9.113}$$

This equation differs from (9.5) is that the coupling constant is now coordinate-dependent and cannot be moved out of the integral. Therefore, it is more convenient to write it explicitly as a function of $\varepsilon(\mathbf{r}')$. Note also that the equation is written for the electric field rather than for polarization $\mathbf{P}(\mathbf{r}) = [(\varepsilon(\mathbf{r}) - 1)/4\pi]\mathbf{E}(\mathbf{r})$.

At the next step, we represent the electrical field inside the sphere as a sum of two contributions:

$$\mathbf{E}(\mathbf{r}) = \mathbf{E}_s(\mathbf{r}) + \mathbf{E}_c(\mathbf{r}) \tag{9.114}$$

where $\mathbf{E}_s(\mathbf{r})$ is the solution to Eq. (9.113) with $\varepsilon_2 = \varepsilon_1$, that is,

$$\mathbf{E}_s(\mathbf{r}) = \mathbf{E}_{\text{inc}}(\mathbf{r}) + \frac{\varepsilon_1 - 1}{4\pi} \int_{V_d} \boldsymbol{G}(\mathbf{r} - \mathbf{r}') \mathbf{E}_s(\mathbf{r}') d^3\mathbf{r}' \tag{9.115}$$

and $\mathbf{E}_c(\mathbf{r})$ is the additional term, which appears because of the presence of a carbon cluster. The parameter $\mathbf{E}_s(\mathbf{r})$ is given by the Mie solution for a dielectric sphere and we assume that it is known. Substituting $\mathbf{E}(\mathbf{r})$ in the form (9.114) into (9.113), we find the equation for $\mathbf{E}_c(\mathbf{r})$:

$$\begin{aligned} \mathbf{E}_c(\mathbf{r}) = {} & \frac{\varepsilon_2 - \varepsilon_1}{4\pi} \int_{V_d} \rho(\mathbf{r}') \boldsymbol{G}(\mathbf{r} - \mathbf{r}') \mathbf{E}_s(\mathbf{r}') d^3\mathbf{r}' \\ & + \int_{V_d} \frac{\varepsilon_1 - 1 + (\varepsilon_2 - \varepsilon_1)\rho(\mathbf{r}')}{4\pi} \boldsymbol{G}(\mathbf{r} - \mathbf{r}') \mathbf{E}_c(\mathbf{r}') d^3\mathbf{r}' \end{aligned} \tag{9.116}$$

The first term in (9.116) with the known function $\mathbf{E}_s(\mathbf{r})$ serves as a free term for the integral equation (9.116).

For many practical problems, a knowledge of the ensemble-averaged interna field is sufficient. (Evidently, this class of problems does not include the problem of nonlinear optics that require consideration of fluctuations of the local field. We cannot perform direct averaging of Eq. (9.116) over random realizations o inclusions, because such averaging would add an additional unknown term $\langle\rho(\mathbf{r})\mathbf{E}_c(\mathbf{r})\rangle$ In the general case, we cannot factorize this correlator as $\langle\rho(\mathbf{r})\mathbf{E}_c(\mathbf{r})\rangle = \langle\rho(\mathbf{r})$ $\langle\mathbf{E}_c(\mathbf{r})\rangle$. However, in the linear (in v_{tot}/v_d) approximation we can neglect the abov term as a higher-order correction. Then, it becomes possible to write an equation fo

the ensemble-average value $\langle \mathbf{E}_c(\mathbf{r}) \rangle$:

$$\langle \mathbf{E}_c(\mathbf{r}) \rangle = \frac{\varepsilon_2 - \varepsilon_1}{4\pi} \int_{V_d} \langle \rho(\mathbf{r}') \rangle \boldsymbol{G}(\mathbf{r} - \mathbf{r}') \mathbf{E}_s(\mathbf{r}') d^3\mathbf{r}' + \frac{\varepsilon_1 - 1}{4\pi} \int_{V_d} \boldsymbol{G}(\mathbf{r} - \mathbf{r}') \langle \mathbf{E}_c(\mathbf{r}') \rangle d^3\mathbf{r}' \tag{9.117}$$

We can draw two important conclusions from the general form of (9.117). First, the ratio of $|\langle \mathbf{E}_c \rangle|/|\mathbf{E}_s|$ is of the same order of magnitude as v_{tot}/v_d. This can be seen by multiplying $\langle \rho(\mathbf{r}') \rangle$ in (9.117) by some arbitrary constant α. The average field $\langle \mathbf{E}_c(\mathbf{r}) \rangle$ is also multiplied by the same factor α. This means that $|\langle \mathbf{E}_c(\mathbf{r}) \rangle|/|\mathbf{E}_s(\mathbf{r})| \sim \langle \rho(\mathbf{r}) \rangle \sim v_{\text{tot}}/v_d$. A similar result is readily obtained for the exact field $\mathbf{E}_c(\mathbf{r})$ (before the averaging).

Second, it is generally impossible to apply the Born expansion or similar perturbation expansion to a calculation of $\langle \mathbf{E}_c(\mathbf{r}) \rangle$. Indeed, both terms on the rhs of (9.117) are of the same order of magnitude (proportional to v_{tot}/v_d). Suppose we start from the zeroth-order approximation $\langle \mathbf{E}_c^{(0)}(\mathbf{r}) \rangle = 0$, and substitute it into (9.117) to obtain the first-order approximation, and so on. It is easy to see that all the terms in the generated expansion will be of the same order of magnitude, and thus convergence cannot be reached.

The above fact makes the general scattering problem for a water droplet containing a cluster inside very complicated. Indeed, the only small parameter of the problem, v_{tot}/v_d, cannot be used to generate a converging expansion for $\mathbf{E}_c(\mathbf{r})$. However, as we show below, we can use the fact that $|\mathbf{E}_c(\mathbf{r})|/|\mathbf{E}_s(\mathbf{r})| \sim v_{\text{tot}}/v_d$ to calculate the absorption cross-section when water itself is weakly absorbing.

The formula for the absorption cross-section in terms of the polarization function can be obtained from the optical theorem and direct integration of the scattering amplitude [34,35], and is analogous to (9.20), except the dielectric function $\varepsilon(\mathbf{r})$ now is not constant inside the integration volume:

$$\sigma_a = \frac{16\pi^2 k}{|\mathbf{E}_0|^2} \int_{V_d} \frac{\operatorname{Im} \varepsilon(\mathbf{r})}{|\varepsilon(\mathbf{r}) - 1|^2} |\mathbf{P}(\mathbf{r})|^2 d^3\mathbf{r} = \frac{k}{|\mathbf{E}_0|^2} \int_{V_d} \operatorname{Im}[\varepsilon(\mathbf{r})] |\mathbf{E}(\mathbf{r})|^2 d^3\mathbf{r} \tag{9.118}$$

By using formulas (9.111) for $\varepsilon(\mathbf{r})$ and (9.114) for $\mathbf{E}(\mathbf{r})$, we can rewrite Eq. (9.118) for the absorption cross-section as

$$\sigma_a = \frac{k \operatorname{Im} \varepsilon_1}{|\mathbf{E}_0|^2} \int_{V_d} |\mathbf{E}_s(\mathbf{r})|^2 d^3\mathbf{r} + \frac{k \operatorname{Im}(\varepsilon_2 - \varepsilon_1)}{|\mathbf{E}_0|^2} \int_{V_d} \rho(\mathbf{r}) |\mathbf{E}_s(\mathbf{r})|^2 d^3\mathbf{r} + \frac{k \operatorname{Im} \varepsilon_1}{|\mathbf{E}_0|^2} \int_{V_d} \{2\operatorname{Re}[\mathbf{E}_s(\mathbf{r}) \cdot \mathbf{E}_c^*(\mathbf{r})] + |\mathbf{E}_c(\mathbf{r})|^2\} d^3\mathbf{r} + \frac{k \operatorname{Im}(\varepsilon_2 - \varepsilon_1)}{|\mathbf{E}_0|^2} \int_{V_d} \rho(\mathbf{r}) \{2\operatorname{Re}[\mathbf{E}_s(\mathbf{r}) \cdot \mathbf{E}_c^*(\mathbf{r})] + |\mathbf{E}_c(\mathbf{r})|^2\} d^3\mathbf{r} \tag{9.119}$$

Now, we analyze the terms on the rhs of (9.119). The first term gives the absorption cross-section by a water droplet without inclusions. It is given by the well-known Mie solution and, consequently, is of no interest to us. Taking into account that $\langle \rho(\mathbf{r}) \rangle \sim |\mathbf{E}_c|/|\mathbf{E}_s| \sim v_{\text{tot}}/v_d$, we find that the second and the third terms are of the same order of magnitude and give the first-order correction to the absorption cross-sections. Finally, the fourth term is of the order of $(v_{\text{tot}}/v_d)^2$, and can be neglected in the first approximation.

Even in the first approximation, the expression for the absorption cross-section contains the unknown field $\mathbf{E}_c(\mathbf{r})$ in the third term of (9.119). However, for the particular case of carbon and water, $\operatorname{Im} \varepsilon_2 \gg \operatorname{Im} \varepsilon_1$. This additional factor allows one to neglect the third term in the expansion (9.119). In principle, the first term can be still large or comparable to the second one due to the large factor v_d/v_{tot}, but this fact does not complicate further derivations.

Finally, we can represent the absorption cross-section as $\sigma_a = \sigma_{a,\text{water}} + \sigma_{a,\text{carbon}}$, where $\sigma_{a,\text{water}}$ is given by the first term in (9.119), and

$$\langle \sigma_{a,\text{carbon}} \rangle = \frac{k \operatorname{Im} \varepsilon_2}{|\mathbf{E}_0|^2} \int_{V_d} \rho(\mathbf{r}) |\mathbf{E}_s(\mathbf{r})|^2 d^3\mathbf{r} \tag{9.120}$$

Formula (9.20) gives the absorption cross-section associated with carbon inclusions in first order in v_{tot}/v_d; the higher corrections are of the order of $(v_{\text{tot}}/v_d)^2$. In the ideal case of $\operatorname{Im} \varepsilon_1 = 0$, this formula gives the total absorption of a composite droplet. Below, we will assume for simplicity that ε_1 is a real number.

Since ρ and $\mathbf{E}_s$ are statistically independent, we can perform direct averaging of (9.120) over random realizations of carbon soot inclusions:

$$\langle \sigma_{a,\text{carbon}} \rangle = \frac{k \operatorname{Im} \varepsilon_2}{|\mathbf{E}_0|^2} \int_{V_d} \langle \rho(\mathbf{r}) \rangle |\mathbf{E}_s(\mathbf{r})|^2 d^3\mathbf{r} \tag{9.121}$$

Note that in the above averaging the radius of a water droplet is fixed.

9.6.3. Enhancement Factor

We define the enhancement factor G as the ratio of the absorption cross-section of a carbon soot cluster in a water microdroplet , defined by (9.121) to that in vacuum:

$$G = \frac{\langle \sigma_{a,\text{carbon}} \rangle}{\langle \sigma_{a,\text{carbon}}^{(0)} \rangle} \tag{9.122}$$

where $\langle \sigma_{a,\text{carbon}}^{(0)} \rangle$ is the average absorption cross-section of carbon soot in vacuum. The latter can be easily calculated using Eq. (9.118) and replacing $\mathbf{E}(\mathbf{r})$ by $\mathbf{E}_{\text{inc}}(\mathbf{r})$. By taking into account that $|\mathbf{E}_{\text{inc}}(\mathbf{r})|^2 = |\mathbf{E}_0|^2$ and $\varepsilon(\mathbf{r}) = 1 + (\varepsilon_2 - 1)\rho(\mathbf{r})$ for carbon

soot in vacuum, we find that $\langle \sigma^{(0)}_{a,\text{carbon}} \rangle = kv \operatorname{Im} \varepsilon_2$ and

$$G = \frac{1}{v_{\text{tot}} |\mathbf{E}_0|^2} \int_{V_d} \langle \rho(\mathbf{r}) \rangle |\mathbf{E}_s(\mathbf{r})|^2 d^3\mathbf{r} \tag{9.123}$$

The average density of carbon inclusions $\langle \rho(\mathbf{r}) \rangle$ must be spherically symmetrical: $\langle \rho(\mathbf{r}) \rangle = \langle \rho(r) \rangle$. Therefore, the angular integration in (9.123) can be done in the most general form, without specifying $\langle \rho \rangle$:

$$G = \frac{1}{v_{tot} |\mathbf{E}_0|^2} \int_0^{R_d} r^2 \langle \rho(r) \rangle dr \int |\mathbf{E}_s(\mathbf{r})|^2 d\Omega \tag{9.124}$$

The internal field $\mathbf{E}_s$ is given by the expansion in terms of the VSHs, $\mathbf{M}_{omn}$, $\mathbf{M}_{emn}$, $\mathbf{N}_{omn}$, and $\mathbf{N}_{emn}$ (for a detailed description of the VSH expansion, see [80]). For a plane incident wave, only the VSHs with $m = 1$ are left in this expansion. Further, if the incident wave is polarized along the x axis, $\mathbf{M}_{e1n}$ and $\mathbf{N}_{o1n}$ are not excited.

For linear absorption, it is sufficient to consider a linear polarization of the incident wave. An elliptical polarization can be described as a superposition of two linearly polarized waves; the absorbed power due to these two waves is added arithmetically because of the linear nature of the interaction. Below, we will adopt the linear polarization of the incident wave along the x axis ($\mathbf{E}_0 = \mathbf{e}_x E_0$), and will use the following simplified notations for the VSHs that can be excited in this particular case: $\mathbf{M}_n \equiv \mathbf{M}_{o1n}$ and $\mathbf{N}_n \equiv \mathbf{N}_{e1n}$. Then, the expansion for the $\mathbf{E}_s$ field takes the form

$$\mathbf{E}_s = \sum_{n=1}^{\infty} i^n \frac{E_0(2n+1)}{n(n+1)} (c_n \mathbf{M}_n - i d_n \mathbf{N}_n) \tag{9.125}$$

Here c_n and d_n are the internal field coefficients [80] defined by

$$c_n = \frac{j_n(x)[x h_n^{(1)}(x)]' - h_n^{(1)}(x)[x j_n(x)]'}{j_n(x_1)[x h_n^{(1)}(x)]' - h_n^{(1)}(x)[x_1 j_n(x_1)]'} \tag{9.126}$$

$$d_n = \frac{j_n(x)[x h_n^{(1)}(x)]' - h_n^{(1)}(x)[x j_n(x)]'}{(x_1/x) j_n(x_1)[x h_n^{(1)}(x)]' - (x/x_1) h_n^{(1)}(x)[x_1 j_n(x_1)]'} \tag{9.127}$$

$$x = kR_d \qquad x_1 = k_1 R_d \qquad k_1 = \sqrt{\varepsilon_1} k \tag{9.128}$$

where $j_n(x)$ and $h^{(1)}(x)$ are the spherical Bessel and Hankel functions of the first kind, respectively, and the prime denotes differentiation with respect to the argument in parentheses.

If we take into account the mutual orthogonality of the VSHs, the angular integral in (9.124) can be written as

$$\int |\mathbf{E}_s(\mathbf{r})|^2 d\Omega = \sum_{n=1}^{\infty} \frac{|E_0|^2 (2n+1)^2}{n^2 (n+1)^2} \left[|c_n|^2 \int \mathbf{M}_n^2 d\Omega + |d_n|^2 \int \mathbf{N}_n^2 d\Omega \right] \tag{9.129}$$

Note that for a purely real dielectric constant ε_1 the VSHs are also real; this is why $|\mathbf{M}_n|^2$ and $|\mathbf{N}_n|^2$ were replaced by $\mathbf{M}_n^2$ and $\mathbf{N}_n^2$ in (9.129).

Integration according to (9.129) can be performed directly using the normalization formulas for the VSHs (the details omitted), and the result is

$$\int |\mathbf{E}_s(\mathbf{r})|^2 d\Omega = 2\pi |E_0|^2 \sum_{n=1}^{\infty} (2n+1) \times \left\{ |c_n|^2 j_n^2(k_1 r) + |d_n|^2 \left[n(n+1) \left(\frac{j_n(k_1 r)}{k_1 r} \right)^2 + \left(\frac{j_n(k_1 r)}{k_1 r} + j_n'(k_1 r) \right)^2 \right] \right\} \tag{9.130}$$

Further calculations require specifying the form of $\langle \rho(r) \rangle$. Below, we consider two cases: fractal distribution of the inclusion density and homogeneous distribution.

An important question is how the carbon inclusions are located inside the microdroplets. This can be influenced by many factors such as the chemical composition of soot particles, surface-tension forces, temperature, and so on. The formation of agglomerates of soot clusters and water can change the geometrical properties of the clusters due to the action of surface-tension forces [81,82]. The average density of inclusions must be spherically symmetrical if there is no distinguished direction in space. We also assume that, in accordance with the fractal density distribution, it obeys a power law with the scaling parameter D according to

$$\langle \rho(r) \rangle = \frac{v_{\text{tot}} D}{4\pi R_d^D} r^{D-3} \quad \text{if} \quad r < R_d \tag{9.131}$$

Here the radius of the microdroplet, R_d, serves as the cutoff, and the density function (9.131) satisfies the normalization (9.112).

Note that, according to its physical meaning as the probability of finding a spo at the distance r from the droplet center occupied by carbon, $\langle \rho(r) \rangle < 1$. In fact the perturbation expansion used above relies on the assumption that $\langle \rho(r) \rangle \ll 1$. The formula (9.131) may seem to contradict this assumption when $r \to 0$. However, the divergence of $\langle \rho(r) \rangle$ at small r is not significant since all the physically importan radial integrals converge fast enough in this limit (see below); thus the actual valu of $\langle \rho(0) \rangle$ is not important. The small parameter of the perturbation expansion, v_{tot}, i obviously present in the definition (9.131).

The case $D = 1$ corresponds to inclusions in the form of long linear sticks, whil $D = 3$ corresponds to a homogeneous distribution of inclusions. If $D = 3$ (trivia geometry), the problem becomes mathematically equivalent to the Mie problem fo a homogeneous dielectric sphere with some effective dielectric constant ε_{eff}. nonperturbative analytic solution can be obtained in this case. However, this metho has certain difficulties. First, the form of ε_{eff} is not obvious. For carbon inclusion of spherical shape and small concentration, one can use $\varepsilon_{\text{eff}} = \varepsilon_1 + (3v_{\text{tot}}/v$

$(\varepsilon_2 - \varepsilon_1)/(\varepsilon_2 + 2\varepsilon_1)$ [83]. But this formula is not applicable when the inclusions are not of spherical shape or form clusters of touching particles. An approach based on determining the effective dielectric function was used by Chowdhury et al. [74,78] who suggested averaging of the ε with the weight that includes the local intensity of the *unperturbed* electric field inside the sphere. Chowdhury et al. define two different averaged dielectric constants, one of which is used for computation of the internal (or external) field coefficients and the other for the effective absorption (or gain). This method is somewhat similar to the perturbative approach used here in that it uses the unperturbed electric field to compute the effective ε. Different effective medium approximations were also used by Videen and Chylek [84]. The second difficulty is that the extinction and scattering cross-sections in the analytical Mie solution are expressed as infinite series involving the scattering coefficient a_n, c_n; the absorption cross-section must be calculated as the difference between these two values. When the absorption is small, such a calculation involves a numerical procedure of finding a small difference between two large numbers, and the round-off errors become very significant. Instead of finding an analytical solution based on some definition of ε_{eff}, we will use the perturbative approach developed above for the $D = 3$ case. This approach is also valid for $D < 3$ (fractal geometry), when an analytical solution cannot be obtained, thus allowing us to maintain self-consistency of the results.

9.6.4. Numerical Results

By using the average density function (9.131), and the result of the angular integration of $|\mathbf{E}_s(\mathbf{r})|^2$ (9.130), one can express the absorption enhancement factor (9.124) in terms of simple radial integrals involving spherical Bessel functions. By inserting the expressions (9.130) and (9.131) into (9.124) and taking the integrals containing derivatives of the spherical Bessel functions by parts, we arrive, after some rearrangement of terms, at the following result:

$$G = \frac{D}{2(k_1 R_d)^D} \sum_{n=1}^{\infty} (2n+1) \left\{ |c_n|^2 I_n(1) + |d_n|^2 \left[\frac{5-D}{2} x_1^{D-2} j_n^2(x_1) + x_1^{D-1} j_n'(x_1) j_n(x_1) + I_n(1) + \frac{(4-D)(3-D)}{2} I_n(3) \right] \right\} \tag{9.132}$$

$$I_n(\alpha) = \int_0^{x_1} x^{D-\alpha} j_n^2(x) dx \tag{9.133}$$

The integrals $I_n(\alpha)$ converge for all physically interesting values of the parameters and must be evaluated numerically, except in the trivial case $D = 3$.

As was pointed out by Bohren and Huffmen [80], the diffraction parameter $x = kR_d$ (or $x_1 = \sqrt{\varepsilon} x$) cannot be, in general, viewed as the only independent variable of the problem, although it may seem so from the mathematical form of Eqs. (9.123) and (9.132). Indeed, when ε_1 depends on λ, $x_1/x \neq$ const. Instead, there are two physically independent parameters that completely define the solution to

the scattering problem: R_d and λ. However, when ε_1 does not de $x_1/x = \varepsilon_1 =$ const, and the diffraction parameter x becomes the only variable. In this case, we do not need to know whether x changes due to R_d or in λ.

For the particular case of water, the assumption $x_1/x =$ const is a g mation in the spectral range from 0.3 to 2.0μm [85]. We have set $\sqrt{}$ const, which allowed us to perform numerical calculation of the enhanc G as a function of one independent variable, $x = kR_d$. We allowed x to 0 to 1000. This range of x includes most of the practical values of R_d and $\lambda = 0.4\,\mu\text{m}$, R_d can vary from 0 to $\approx 60\,\mu\text{m}$.

Now, we turn to the calculation of the internal field coefficients, c_n calculated the Bessel functions and their first derivatives that are definitions (9.126) and (9.127) of the internal field coefficients, using th recursion relation [86]. The maximum order n that gives significant co the optical cross-sections can be roughly estimated [80] as $n_{\max} \approx$ internal field coefficients $|c_n|^2$ and $|d_n|^2$ decrease dramatically for illustrated in Fig. 9.14. In Fig. 9.14(a), we plot the internal field co $\sqrt{\varepsilon_1} = 1.33$ and $x = 259.664$. The specific value of x was chosen from that the absorption cross-section has a resonance. In terms of th resonance occurs for the order $n = 131$, when $|c_n|^2$ reaches the value 10^7; there is also a large number of weaker resonances of $|c_n|^2$. (Note no strong resonances.) Since the total number of VSHs that cont absorption is of the order of 300, and $|c_{131}|^2$ is more than five orders larger than the average background, we can conclude that the resona the prevailing input to the optical cross-sections. For comparison, w 9.14(b) the internal field coefficients for the same refraction index, b resonant value of $x = 260.400$. Both pictures look very similar, ap resonance order $n = 131$ in Fig. 9.14(a).

The numerical results for the absorption enhancement factor $G(x)$ Fig. 9.15 for $D = 1.1$ [Fig. 9.15(a)] and $D = 3.0$ [Fig. 9.15(b)]. As c Fig. 9.15, $G(x)$ has a large number of quasirandom morphology-depen ces (due to the presence of resonances in the internal field coefficients Fig. 9.14), but only a very slight systematic dependence of $G(x)$ on x the interval $10 < x < 1000$. The slight systematic increase of $G(x)$ ca to an increase in the average resonance quality with the size paramet also seen from a comparison of Figs. 9.15(a) and (b) that the enhance larger, on average, for $D = 1.1$ than for $D = 3.0$.

In a polydisperse ensemble of microdroplets with size parameter range $10 < x < 1000$ the individual resonances are smoothed out an absorption enhancement factor, $\langle G \rangle$, which is practically important, i averaging of $G(x)$ over x. We performed such averaging in the interval above for different D ($1 \leq D \leq 3$) and the results are shown in F averaging was performed with the step size in x equal to 0.1. This step enough so that most resonances were visually resolved. Averaging resolution resulted in a smaller value of $\langle G \rangle$ because the resonances in

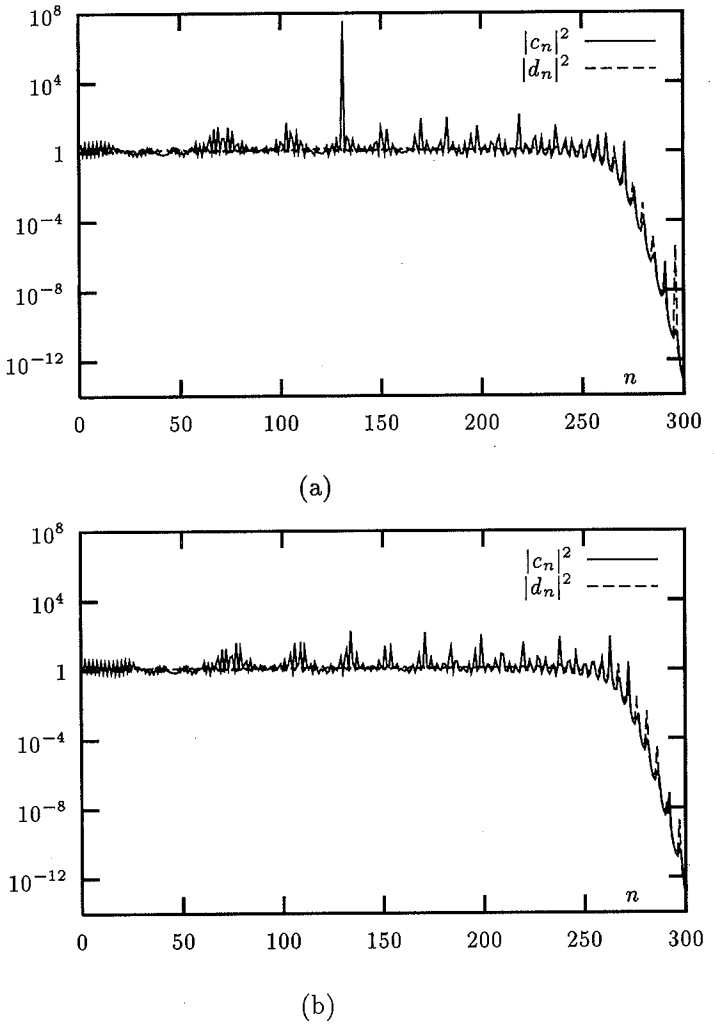

Figure 9.14. Internal field coefficients, $|c_n|^2$ and $|d_n|^2$, as functions of the VSH order, n. (a): $x = 259.664$ (resonance order $n = 131$); (b): $x = 260.400$ (no pronounced resonances).

narrow. It is important to emphasize the significance of the averaging process. For a randomly chosen x, $G(x)$ is, with a large probability, less than $\langle G \rangle$ by a factor of 4 or 5. Thus the resonances of $G(x)$ play an important role and should not be ignored. It should be noted that the averaging was performed in the region of $10 < x < 1000$, where there is no pronounced systematic dependence of $G(x)$ on x. For $x < 10$, the averaged G is considerably smaller.

As can be seen in Fig. 9.16, $\langle G \rangle$ is maximum for $D = 1$ and decreases toward $D = 3$. For the practically important value $D = 1.8$, $\langle G \rangle \approx 16$, and the maximum variation of $\langle G \rangle$ with D, does not exceed ± 6. The dependence of $\langle G \rangle$ on D can be

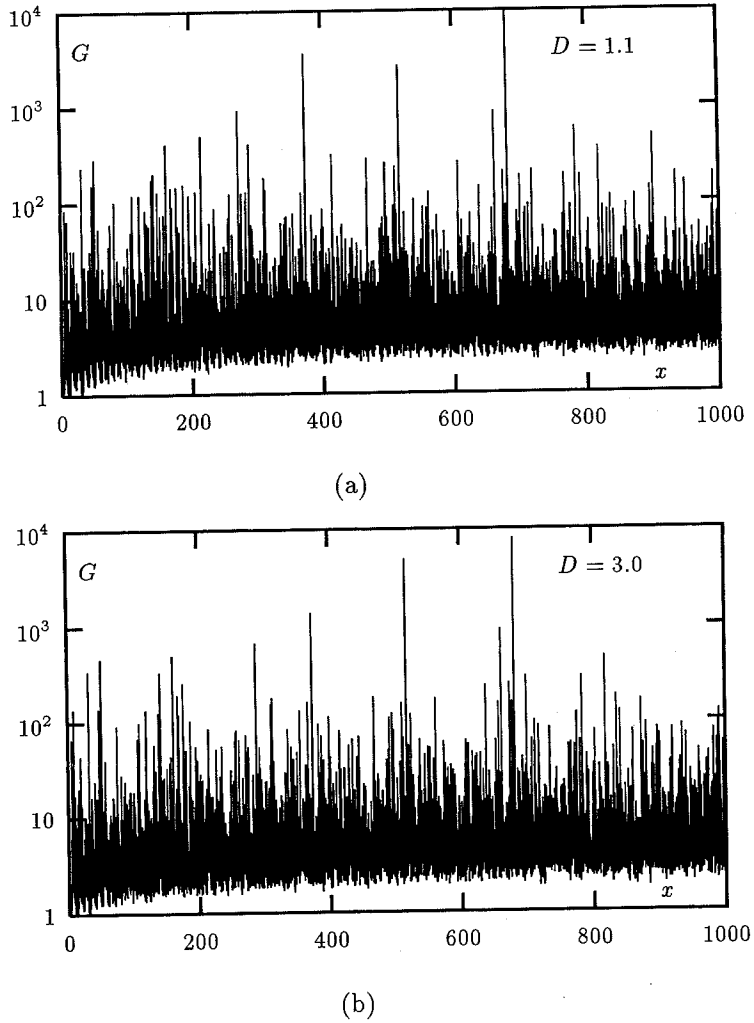

Figure 9.15. Absorption enhancement factor G as a function of the diffraction parame $x = kR_d$ for $D = 1.1$ (a) and $D = 3.0$ (b).

explained by an interference between the fractal density function $\langle \rho(r) \rangle$ and t modes of a spherical resonator.

The averaging procedure involved in our calculations might explain why estimates of the enhancement factor are significantly larger than those repor earlier [52,79,84,87]. Fuller calculated the specific absorption cross-section fo single spherical carbon grain located near the surface of a water droplet [52] a inside the water droplet [79] as a function of the grain's position. Although Fulle data are not averaged over the whole volume of the microdroplet, they indicate t the volume-averaged absorption enhancement factor is < 14. Chylek et al. [

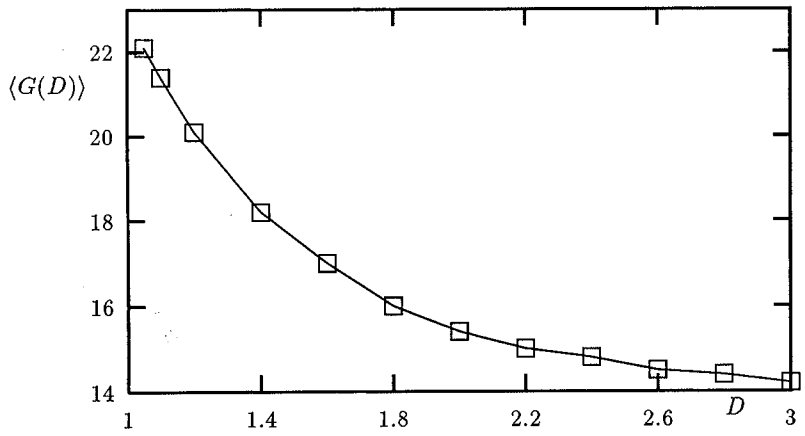

Figure 9.16. Average absorption enhancement factor $\langle G \rangle$ as a function of the fractal dimension, D.

averaged the same quantity for the carbon inclusion location distributed evenly within a spherical cone with the axis collinear to the incident wave propagation direction and over the whole volume [84]. In the first case, the authors estimate the enhancement factor to be ≈ 4, and in the second ≈ 2. However, all of the above calculations were performed for a fixed value of the diffraction parameter x. Because the resonances are very narrow, it is unlikely that a randomly selected value of x will lie within a resonance. Our calculations indicate that if x is chosen exactly in resonance, the volume-averaged enhancement factor can be as large as 10^4. Our calculations indicate that the averaged absorption factor is larger by a factor of $\sim 4-5$ than that calculated for a randomly selected value of x. For the trivial distribution of carbon inclusions ($D = 3$), we obtain the averaged enhancement factor of 14, while for a randomly selected value of x the typical (most probable) enhancement factor is from 2 to 4. This suggests that, although the resonances in x are very narrow, they are not small in the integral sense, and should be taken into account.

In conclusion, we note that within the framework of the first Born approximation that was used throughout this section, the absorption cross-section of a free carbon soot cluster excited by a plane wave is proportional to the total volume of carbon and does not depend on the cluster's geometrical configuration. However, this is not the case when the cluster is excited by the inhomogeneous modes of a spherical resonator instead of plane waves. In this case, the absorption is stronger, on average, if the inclusions tend to concentrate in the spatial regions where the intensity of local fields is higher.

ACKNOWLEDGMENTS

This research was supported by Battelle under Contract DAAH04-96-C-0086. It was partially supported by National Computational Science Alliance under Grant PHY980006N and utilized the NCSA HP/Convex Exemplar SPP-2000. The authors are grateful to D. Mackowski for making his Fortran codes available and to E. Mikhailov, S. Vlasenko, and A. Kiselev for providing digital images of fractal soot aggregates.

REFERENCES

1. C. W. Bruce, T. F. Stromberg, K. P. Gurton, and J. B. Mozer, *Appl. Opt.* ***30***, 1537 (1991).
2. W. H. Dalzel, G. C. Williams, and H. C. Hottel, *Combust. Flame* ***14***, 161 (1970).
3. S. R. Forrest and T. A. Witten, *J. Phys. A* ***12***, L109 (1979).
4. R. D. Mountain and G. W. Mulholland, in F. Family and D. P. Landau, Eds., *Kinetics, of Aggregation and Gelation*, North-Holland, Amsterdam, 1984, pp. 83–86.
5. U. O. Koylu and G. M. Faeth, *Combust. and Flame* ***89***, 140 (1992).
6. E. F. Mikhailov and S. S. Vlasenko, *Phys. Usp.* ***165***, 253 (1995).
7. H. X. Zhang et al., *Langmuir* ***4***, 867 (1988).
8. J. Cai, N. Lu, and C. M. Sorensen, *Langmuir* ***9***, 2861 (1993).
9. U. O. Koylu, G. M. Faeth, T. L. Farias, and M. G. Carvalho, *Combust. Flame* ***100***, 621 (1995).
10. T. T. Charalampopoulos and H. Chang, *Combust. Flame* ***87***, 89 (1991).
11. J. Cai, N. Lu, and C. M. Sorensen, *J. Colloid Interface Sci.* ***171***, 470 (1995).
12. P. Meakin, *Phys. Rev. Lett.* ***51***, 1119 (1983).
13. R. Jullien, M. Kolb, and R. Botet, *J. Phys. Lett. (Paris)* ***45***, L211 (1984).
14. J. E. Martin and A. J. Hurd, *J. Appl. Crystallogr.* ***20***, 61 (1987).
15. V. A. Markel, V. M. Shalaev, E. Y. Poliakov, and T. F. George, *Phys. Rev. E* ***55***, 7313 (1997).
16. C. Amitrano, A. Coniglio, P. Meakin, and M. Zannetti, *Phys. Rev. B* ***44***, 4974 (1991).
17. R. D. Mountain and G. W. Mulholland, *Langmuir* ***4***, 1321 (1988).
18. C. Oh and C. M. Sorensen, *J. Colloid Interface Sci.* ***193***, 17 (1997).
19. M. K. Wu and S. K. Friedlander, *J. Colloid Interface Sci.* ***159***, 246 (1993).
20. M. V. Berry and I. C. Percival, *Opt. Acta* ***33***, 577 (1986).
21. C. M. Sorensen, N. Lu, and J. Cai, *J. Colloid Interface Sci.* ***174***, 456 (1995).
22. C. M. Sorensen, C. Oh, P. W. Schmidt, and T. P. Rieker, *Phys. Rev. E* ***58***, 4666 (1998).
23. V. A. Markel, V. M. Shalaev, E. Y. Poliakov, and T. F. George, *J. Opt. Soc. Am. A* ***14***, 60 (1997).
24. S. M. Rytov, Y. A. Kravtsov, and V. I. Tatarskii, *Elements of Random Fields*, Vol. 3 of *Principles of Statistical Radiophysics*, Springer-Verlag, Berlin, 1989.
25. S. M. Rytov, Y. A. Kravtsov, and V. I. Tatarskii, *Wave Propagation through Random Media*, Vol. 4 of *Principles of Statistical Radiophysics*, Springer-Verlag, Berlin, 1989.
26. W. H. Dalzell and A. F. Sarofim, *J. Heat Transfer* ***91***, 100 (1969).
27. E. A. Taft and E. A. Philipp, *Phys. Rep.* ***138***, A197 (1965).
28. Z. G. Habib and P. Vervisch, *Combust. Sci. Technol.* ***59***, 261 (1988).
29. S. C. Lee and C. L. Tien, in *Eighteenth Symposium (International) on Combustion*, The Combustion Institute, 1981, pp. 1159–1166.

30. V. A. Markel, L. S. Muratov, and M. I. Stockman, *Sov. Phys. JETP* ***71***, 455 (1990).
31. V. A. Markel, L. S. Muratov, M. I. Stockman, and T. F. George, *Phys. Rev. B* ***43***, 8183 (1991).
32. G. W. Mulholland, C. F. Bohren, and K. A. Fuller, *Langmuir* ***10***, 2533 (1994).
33. G. W. Mulholland and R. D. Mountain, *Combust. Flame* ***119***, 56 (1999).
34. V. A. Markel, *J. Opt. Soc. Am. B* ***12***, 1783 (1995).
35. V. A. Markel and E. Y. Poliakov, *Philos. Mag. B* ***76***, 895 (1997).
36. J. D. Jackson, *Classical Electrodynamics*, Wiley, New York, 1975.
37. V. M. Shalaev, R. Botet, and R. Jullien, *Phys. Rev. B* ***44***, 12216 (1991).
38. E. M. Purcell and C. R. Pennypacker, *Astrophys. J.* ***186***, 705 (1973).
39. B. T. Draine, *Astrophys. J.* ***333***, 848 (1988).
40. B. Draine and P. Flatau, *J. Opt. Soc. Am. A* ***11***, 1491 (1994).
41. V. A. Markel, *J. Mod. Opt.* ***39***, 853 (1992).
42. J. M. Gerardy and M. Ausloos, *Phys. Rev. B* ***22***, 4950 (1980).
43. F. Claro, *Phys. Rev. B* ***25***, 7875 (1982).
44. J. E. Sansonetti and J. K. Furdyna, *Phys. Rev. B* ***22***, 2866 (1980).
45. F. Claro, *Phys. Rev. B* ***30***, 4989 (1984).
46. F. Claro, *Solid State Commun.* ***49***, 229 (1984).
47. R. Rojas and F. Claro, *Phys. Rev. B* ***34***, 3730 (1986).
48. R. Fuchs and F. Claro, *Phys. Rev. B* ***35***, 3722 (1987).
49. D. W. Mackowski, *Appl. Opt.* ***34***, 3535 (1995).
50. D. W. Mackowski and M. Mischenko, *J. Opt. Soc. Am. A* ***13***, 2266 (1996).
51. K. A. Fuller, *J. Opt. Soc. Am. A* ***11***, 3251 (1994).
52. K. A. Fuller, *J. Opt. Soc. Am. A* ***12***, 881 (1995).
53. Y.-l. Xu, *Appl. Opt.* ***34***, 4573 (1995).
54. V. A. Markel et al., *Phys. Rev. B* ***53***, 2425 (1996).
55. V. A. Markel and V. M. Shalaev, in D. A. Jelski and T. F. George, Eds., *Computational Studies of New Materials*, World Scientific, Singapore, 1999, pp. 210–243.
56. V. A. Markel, *J. Mod. Opt.* ***40***, 2281 (1993).
57. M. K. Singham, S. B. Singham, and G. C. Salzman, *J. Chem. Phys.* ***85***, 3807 (1986).
58. Y. E. Danilova, Ph.D. Thesis, Institute of Automation and Electrometry, SB RAS, Novosibirsk, 1999.
59. P. Chylek, V. Ramaswamy, and R. J. Cheng, *J. Atm. Sci.* ***41***, 3076 (1984).
60. R. E. Danielson, D. R. Moore, and H. C. Van Hulst, *J. Atm. Sci.* ***26***, 1078 (1969).
61. H. Grassl, *Contrib. Atm. Phys.* ***48***, 199 (1975).
62. S. Twomey, *J. Atm. Sci.* ***33***, 1087 (1976).
63. K. Y. Kondratyev, V. I. Binenko, and O. P. Petrenchuk, *Izv. Akad. Nauk (USSR) Fiz. Atm. Okeana* ***17***, 122 (1981).
64. V. A. Markel and V. M. Shalaev, *J. Quant. Spectrosc. Rad. Transfer* ***63***, 321 (1999).
65. H.-B. Lin et al., *Opt. Lett.* ***17***, 970 (1992).
66. P. Chylek, D. Ngo, and R. G. Pinnik, *J. Opt. Soc. Am. A* ***9***, 775 (1992).
67. R. L. Armstrong et al., *Opt. Lett.* ***18***, 119 (1993).

68. J.-G. Xie, T. E. Ruekgauer, R. L. Armstrong, and R. G. Pinnik, *Opt. Lett.* ***18***, 340 (1993).
69. J. Gu, T. E. Ruekgauer, J.-G. Xie, and R. L. Armstrong, *Opt. Lett.* ***18***, 1293 (1993).
70. D. Ngo and R. G. Pinnik, *J. Opt. Soc. Am. A* ***11***, 1352 (1994).
71. M. Kerker, D. D. Cooke, H. Chew, and P. J. McNulty, *J. Opt. Soc. Am.* ***68***, 592 (1978).
72. F. Borghese, P. Denti, R. Saija, and O. I. Sindoni, *J. Opt. Soc. Am. A* ***9***, 1327 (1992).
73. M. M. Mazumder, S. C. Hill, and P. W. Barber, *J. Opt. Soc. Am. A* ***9***, 1844 (1992).
74. D. Q. Chowdhury, S. C. Hill, and M. M. Mazumder, *IEEE J. Quantum Electron.* ***29***, 2553 (1993).
75. F. Borghese, P. Denti, and R. Saija, *Appl. Opt.* ***33***, 484 (1994).
76. K. A. Fuller, *Opt. Lett.* ***19***, 1272 (1994).
77. S. C. Hill, H. I. Saleheen, and K. A. Fuller, *J. Opt. Soc. Am. A* ***12***, 905 (1995).
78. D. Q. Chowdhury, S. C. Hill, and M. M. Mazumder, *Opt. Commun.* ***131***, 343 (1996).
79. K. A. Fuller, *J. Opt. Soc. Am. A* ***12***, 893 (1995).
80. C. F. Bohren and D. R. Huffman, *Absorption and Scattering of Light by Small Particles*, Wiley, New York, 1983.
81. E. F. Mikhailov, S. S. Vlasenko, T. I. Ryshkevitch, and A. A. Kiselev, *J. Aerosol Sci.* ***27***, S709 (1996), suppl. 1.
82. E. F. Mikhailov, S. S. Vlasenko, A. A. Kiselev, and T. I. Ryshkevich, in M. M. Novak and T. G. Dewey, Eds., *Fractal Frontiers*, World Scientific, Singapore, 1997, pp. 393–402.
83. L. D. Landau and L. P. Lifshitz, *Electrodynamics of Continuous Media*, Pergamon Press, Oxford, 1984.
84. G. Videen and P. Chylek, *Opt. Commun.* ***158***, 1 (1998).
85. I. Thormahlen, J. Straub, and U. Grigull, *J. Phys. Chem. Ref. Data* ***14***, 933 (1985).
86. H. Bateman, *Higher Transcendental Functions*, Vol. 2, McGraw-Hill, New York, 1953.
87. P. Chylek et al., *J. Geophys. Res.* ***101***, 23365 (1996).